Research papers

Improving snow simulation with more realistic vegetation parameters in a regional climate model in the Tianshan Mountains, Central Asia

Tao Yang [a,b,c,d,e,f], Qian Li [a,b,c,g,*], Xi Chen [a,c,e,g], Rafiq Hamdi [h], Philippe De Maeyer [d,e,f,i], Alishir Kurban [a,e,f], Lanhai Li [a,b,c,g,j,*]

[a] State Key Laboratory of Desert and Oasis Ecology, Xinjiang Institute of Ecology and Geography, Chinese Academy of Sciences, Urumqi 830011, China
[b] Ili Station for Watershed Ecosystem Research, Chinese Academy of Sciences, Xinyuan 835800, China
[c] University of Chinese Academy of Sciences, Beijing 100049, China
[d] Department of Geography, Ghent University, 9000 Ghent, Belgium
[e] Sino-Belgian Joint Laboratory of Geo-information, Urumqi 830011, China
[f] Sino-Belgian Joint Laboratory of Geo-information, 9000 Ghent, Belgium
[g] CAS Research Centre for Ecology and Environment of Central Asia, Urumqi 830011, China
[h] Meteorological and Climatological Department, Royal Meteorological Institute, Brussels, Belgium
[i] Xinjiang Institute of Ecology and Geography, Chinese Academy of Sciences, Urumqi 830011, China
[j] Xinjiang Key Laboratory of Water Cycle and Utilization in Arid Zone, Urumqi 830011, China

ARTICLE INFO

ABSTRACT

The snowpack evolution has a significant impact on the water cycle and energy exchange at the watershed and regional scales, especially in the mountainous area with complex topography and land surface properties. An accurate description of the vegetation parameters for the regional climate model (RCM) coupled with the land surface model (LSM) is necessary to achieve a more accurate simulation of the mountainous snow process. However, the default vegetation options could not update real-time in the RCM LSMs, causing large uncertainties in the snow mass estimation. Thus, this study investigated the effect of the key vegetation parameters on the snow simulation in the Tianshan Mountains (TS) through real-time updates with remotely sensed leaf area index (LAI), green vegetation fraction (FVEG) and land cover (LC) products in the Weather Research and Forecasting (WRF) model coupled with the Noah LSM with Multiparameterization Options (Noah-MP). The results demonstrated that more realistic vegetation parameters could improve the performance of snow simulation in the WRF/Noah-MP, especially in the forest regions. The underestimated vegetation parameters of the integrated remote sensing products caused an increased surface albedo and less snow interception, particularly in the snow ablation period, and less vegetation density could also reduce the net longwave radiation emitted from the canopy at the surface, causing a lower near-surface temperature and less snowmelt. Additionally, less snow interception and melted snow contributed to a larger snow water equivalent on the ground, such as in the Western TS and the high-altitude regions of the Ili Valley. The updating vegetation parameters' approach will help to provide information so as to accurately model the snow resources in the mountainous areas.

1. Introduction

The seasonal snowpack is a critical component of the freshwater storage in the mountainous regions, playing an important role in the regional water cycle and water consumption for the agricultural and economic development (Barnett et al., 2005; Dong, 2018; Matthew et al., 2017). Due to the high albedo and excellent thermal insulation, snow also has a significant influence on the climate system by affecting the land–atmosphere energy exchange (Bair et al., 2019; Brown and Mote, 2009; Malmros et al., 2018; Winter et al., 2017). The alpine vegetation phenology in spring is influenced by the snow cover duration and snow mass (Tomaszewska et al., 2020; Wang et al., 2013, 2018). In addition, snow also brings natural disasters such as blowing snow and snow avalanches which cause huge damage and economic losses (Ballesteros-Cánovas et al., 2018; Schweizer et al., 2003). Therefore, it is necessary and meaningful to estimate the snow mass in

* Corresponding authors at: State Key Laboratory of Desert and Oasis Ecology, Xinjiang Institute of Ecology and Geography, Chinese Academy of Sciences, Urumqi 830011, China.
E-mail addresses: liqian@ms.xjb.ac.cn (Q. Li), lilh@ms.xjb.ac.cn (L. Li).

the mountainous areas accurately.

The current snow measurement approach is mainly based on the in-situ observations, remote sensing and model simulations (Dong, 2018). The point-based snow observation is sparse, especially in the mountainous areas and forest transitions (Broxton et al., 2019). In addition, the in-situ snow water equivalent (SWE) measurement is performed at a low frequency (Dong, 2018). During the past decades, remote sensing has proven to be an effective approach to investigate snow (DeWalle and Rango, 2008). Although the optical remote sensing has been widely used to map the snow cover, the quality of the estimation depends on the cloud cover and has a limited detection of snow depth (SD) (Hall et al., 2010; Huang et al., 2018). Microwave remote sensing could monitor the snow mass without the influence of the cloud cover and winter darkness. The long repeat-pass interval (Lievens et al., 2019), and the coarse spatial resolution and complex influencing factors (Dai et al., 2017; Immerzeel et al., 2009) lead to large uncertainties in snow mass estimation using the active microwave and passive microwave sensors, respectively. The LSMs with a snow physics module could simulate the snow accumulation and ablation processes. However, it is a hard challenge to perform adequately snow dynamics due to the requirements on multi-parameters and accurate meteorological forcing data in the mountainous areas (Alonso-González et al., 2018; Pan et al., 2003; Wrzesien et al., 2018).

Recently, the RCMs coupled LSMs were successfully applied to estimate the mountain snowpack storage through more reasonable simulation of the orographic precipitation at a high spatial resolution in a given domain (Chen et al., 2014; Leung and Qian, 2003; Minder et al., 2016). For example, the WRF model (Skamarock and Klemp, 2008) coupled with the Noah-MP (Niu et al., 2011) model has effectively captured the snow dynamics in the mountain area (Liu et al., 2019; Tomasi et al., 2017). As an essential structure of the RCM LSMs, the vegetation has an important impact on the snow process (Essery et al., 2009; Roth and Nolin, 2017; Todt et al., 2019). Vegetation intercepts the snowfall during the snow accumulation season, reducing the surface ground snow under the canopy (Hedstrom and Pomeroy, 1998; Helbig et al., 2019). In addition, vegetation reduces the albedo and augments the radiation absorption, affecting the longwave radiation that is transmitted under the vegetation and impacting the snowmelt and revolution (Essery, 2013; Niu and Yang, 2004). The vegetation parameters, such as the LC, LAI and FVEG constitute the key parameters in the RCM LSMs of the land surface and phenology (Corporation et al., 2018; Xu et al., 2014). However, these parameters are mainly based on the look-up table or climatology of the remote sensing products, indicating that they could not be updated in real-time (Gou et al., 2019; Wen et al., 2012). Previous studies demonstrated that more realistic vegetation parameters from real-time remote sensing data of LAI, FVEG, and LC could better reflect the land and atmosphere interactions (Cao et al., 2019; Ge et al., 2020; Kumar et al., 2019). Nevertheless, the changes in snow simulation caused by the vegetation parameters did not sufficiently attract attention using the RCM LSMs in the mountainous area.

Situated in the hinterland of the Eurasian continental climate zone, the Tianshan Mountains (TS) are called the water tower of Central Asia and function as an ecological barrier (Chen et al., 2016). Major rivers (e.g. the Ili River, Tarim River, Chu River and Syr Darya River) originate from the TS and provide large proportions of glaciers/snowmelt water for the oasis-desert ecosystem (Chen et al., 2018), creating one of the largest irrigational areas worldwide (Farinotti et al., 2015; Sorg et al., 2012). The accurate estimation of SD and SWE has a significance to the surrounding water resources, agriculture and ecosystem (Yang et al., 2019a; Zhang et al., 2016). Since the meteorological observations are sparse (Yang et al., 2020), especially in the high-altitude and forest regions, most studies investigated the variability of the snow cover by means of optical remote sensing in the entire or part of the TS (Tang et al., 2017; Wu et al., 2019; Zhou et al., 2017). A few studies that were based on the in-situ observations focused on the variations of the SD

and snow phenology in the areas within China (Li et al., 2019, 2018b). Recently, the SD and SWE have been simulated by the Noah-MP only on a point scale (You et al., 2020a, You et al., 2020b). In addition, microscale research demonstrated that the differences in forest canopy openness could cause changes in the energy budget of the snow surface, particularly in the snowmelt season (Lu et al., 2017). However, little is known about the impact of the vegetation on the snow simulation in the entire TS. Hence, it is expected that the accurate vegetation parameters could improve the performance of the snow simulation using the RCM LSMs in the TS.

This study aimed at investigating the impacts of various vegetation parameter datasets (LC, LAI and FVEG) on snow by means of the WRF/Noah-MP in the TS from 2005 to 2015. The objectives of the study are as following: (1) to evaluate the performance of snow simulation in the WRF/Noah-MP; (2) to investigate the spatial distribution of the SD and SWE; (3) to discuss the effect of different vegetation parameter sources on the snow process. This is the first attempt to estimate the snow mass using the RCM LSMs and to investigate the differences in snow simulation caused by the vegetation parameters over the entire TS. The results will help to enhance understanding of the vegetation effect on snow simulation and will give new insight in order to improve the snow process in the RCM LSMs.

2. Data and methods

2.1. Study area

The TS measure approximately 2,500 km in length and has a width of 250–350 km, spanning from Xinjiang (China), southeastern Kazakhstan and Uzbekistan to Kyrgyzstan with 800,000 km^2 and developed the largest mountain system in Central Asia (Fig. 1b). The westerlies and complex topography bring abundant precipitation which is beneficial to form the rich glaciers and snow resources. The lowland area of the TS is one of the largest irrigated zones worldwide, and its agriculture and economy are highly dependent on the glaciers/snow melting water (Farinotti et al., 2015). The mean annual temperature and annual precipitation amount are 4.6 °C and 329.3 mm, respectively (Yang et al., 2019a). The western and northern part of the TS is characterized by a relatively humid climate, while the eastern and central parts exhibit a typical continental climate (Farinotti et al., 2015). The annual precipitation reaches 500–700 mm and 1,000 mm along the northern slope of the TS (NTS) and the windward slope of the western part, respectively, but below 100 mm in the southern slope of the TS (STS) (Lu et al., 2019). The snowfall amount accounts for 30% of the annual precipitation in the NTS (Guo and Li, 2015; Yang et al., 2019b). The maximum precipitation period in the western part occurs in late winter to early spring, which is earlier than that in the central part in summer, the northern and eastern part in spring and early summer (Aizen et al., 1997). Leptosol, Gypsisol, Kastanozem, Solonchak and Chernozem are the main soil types in this area (Fao/Iiasa/Isric/Isscas/Jrc, 2012). As illustrated in Fig. 1e, the TS is dominated by barren land, grassland cropland, and shrubland in CCI-LC 2015, accounting for 55.1%, 21.2%, 13.0%, and 6.1% of total land areas, respectively. The forest cover (1.2%) is mainly distributed in the altitude zone from 1,300 m to 2, 800 m (Lu et al., 2017).

2.2. Datasets' acquisition and processing

2.2.1. Meteorological observations and Terrestrial water storage product

The data from the meteorological stations and satellite were used to evaluate the performance of the WRF/Noah-MP. There are 95 meteorological stations in the study area (shown in Fig. 1b). These data have been strictly processed and subjected to quality control before release. Fifty-nine stations were collected from the China Meteorological Administration (CMA, http://data.cma.cn/site/index.html), which includes the mean daily temperature, precipitation, snow depth and a 5-
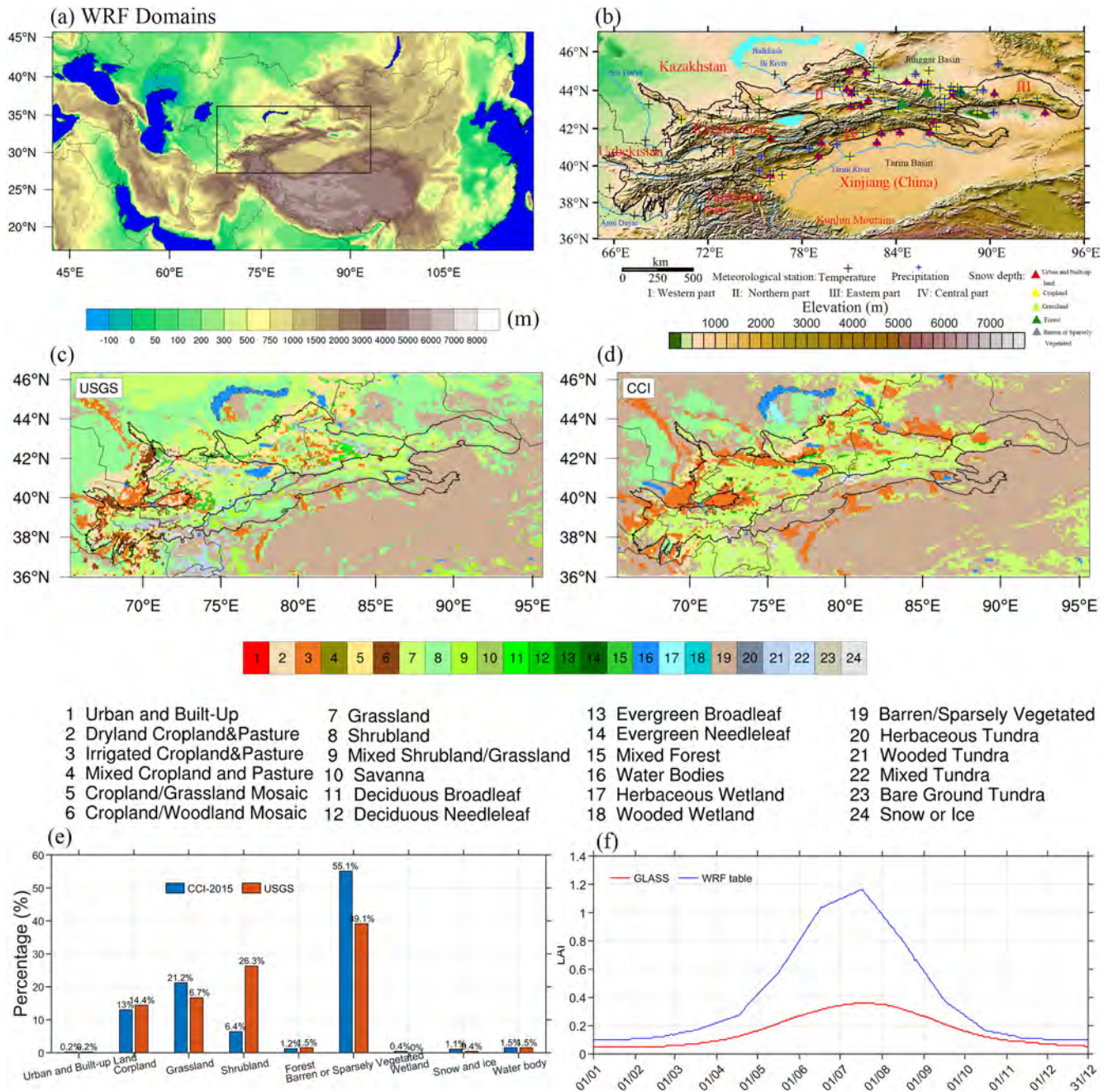
Fig. 1. (a) Elevation (m) of the WRF model domains; (b) Location of the Tianshan Mountains, (c) default USGS land use, (d) CCI_LC (2015) land use, (e) land-cover types fraction, and (f) Multi-year averaged LAI from the WRF look-up table and GLASS dataset in d02.

day SWE (SWE is recorded once every 5 days when SD > 5 cm). Thirty-three stations were obtained from the Global Surface Summary of the Day (GSOD, https://data.nodc.noaa.gov/cgi-bin/iso?id=gov.noaa.ncdc:C00516). All GSOD stations cover the mean daily temperature, of which only 3 stations contain daily snow depth data. Details are visible in Table 1. The average daily temperature, SD, and precipitation in the cold season (from November to March) from the in-situ observations were applied so as to evaluate the performance of the WRF/Noah-MP simulations.

Due to a lack of observations in the forest regions, the daily SD and 5-day SWE at the Tianshan Station for Snow Cover and Avalanche Research (TSSAR), Chinese Academy of Sciences, and the daily SD at the Baiyanggou (BYG) and Tianchi (TC) station obtained from the Xinjiang Meteorological Bureau were employed to validate the vegetation impact on the snowpack simulation (Table 2 and Fig. 1b). In

addition, changes in the Terrestrial Water Storage (TWS) during the cold season are dominated by snow accumulation or melting in the mountainous regions (Wrzesien et al., 2018). In order to evaluate the SWE simulation during the cold season in the TS, the Gravity Recovery and Climate Experiment (GRACE) monthly TWS anomaly product (version RL06) at a 0.5° spatial resolution from 2005 to 2015 (https://grace.jpl.nasa.gov/data/get-data/) was utilized to compare with the TWS anomaly estimated by the WRF/Noah-MP. The GRACE measurement error of water-equivalent height was < 25 mm in the midlatitude region (Landerer and Swenson, 2012; Wahr et al., 2006). The sum of the soil moisture, groundwater storage, SWE and canopy water contents is defined as the TWS in the Noah-MP model (Kumar et al., 2019).

2.2.2. Remotely sensed vegetation products

The LC and LAI datasets have been obtained from the European

Table 1
The CMA and GSOD meteorological stations in the TS.

	ID	Longitude (°E)	Latitude (°N)	Altitude (m)	ID	Longitude (°E)	Latitude (°N)	Altitude (m)	
NTS	51,232	82.57	45.18	338	51,644	83.07	41.72	1,083	
	51,238#	82.07	44.9	533	51,656	86.13	41.75	933	
	51,288	90.53	45.37	1,655	51,701	75.4	40.52	3,507	
	51,328	80.42	44.2	774	51,704	76.17	39.72	1,300	
	51,329	80.85	44.05	641	51,705	75.25	39.72	2,178	
	51,330#	81.02	44.97	1,354	51,707	76.73	39.5	1,211	
	51,334#	82.9	44.62	321	51,708	75.95	39.15	1,325	
	51,346#	84.67	44.43	478	51,709	75.98	39.47	1,291	
	51,352	85.25	44.85	338	51,711#	78.45	40.93	1,986	
	51,353	86.1	45.02	348	51,716	78.57	39.8	1,118	
	51,356#	86.05	44.32	444	51,720	79.05	40.5	1,163	
	51,357	85.62	44.33	523	51,730	81.05	40.5	1,013	
	51,358	85.82	44.28	469	52,203	93.52	42.82	739	
	51,359	86.2	44.32	473	368,210	76.27	44.83	396	
	51,365	87.53	44.2	441	368,590	80.07	44.17	645	WTS
	51,367	86.82	44.13	524	368640*	75.25	43.53	743	
	51,368#	87.43	44.02	579	369,110	75.28	42.83	817	
	51,369	87.65	43.97	601	369740*	76	41.43	2,041	
	51,377	87.92	44.17	548	369,820	78.23	41.88	3,639	
	51,378	89.17	44.02	736	381,960	68.9	43.55	822	
	51,379#	89.57	44.02	794	381,980	68.22	43.27	207	
	51,430	81.15	43.83	604	382,220	73.78	43.7	456	
	51,431#	81.33	43.95	663	383,280	69.7	42.32	640	
	51,433#	82.57	43.8	1,106	383340*	70.3	42.48	808	
	51,434	81.53	43.97	771	383,410	71.38	42.85	655	
	51,435	82.23	43.47	777	383,430	72.75	42.95	683	
	51,436#	83.3	43.45	929	383,450	72.22	42.52	1,218	
	51,437#	81.13	43.15	1,855	383,530	74.53	42.85	760	
	51,438	81.77	43.18	1,211	383,531	74.48	43.06	627	
	51,463#	87.65	43.78	936	384,390	68	41.37	275	
	51,465#	87.1	43.57	2,121	384,570	69.28	41.26	432	
	51,467	86.3	42.73	1,740	384,620	70.37	41.9	1,258	
	51,468	86.83	43.1	3,544	385,650	65.68	40.55	485	
	51,469	87.11	43.27	1,930	385,790	67.83	40.12	345	
	51,482	90.28	43.83	1,272	385,830	68.68	40.82	264	
	52,101#	93	43.6	1,651	385,990	69.73	40.22	427	
	51,542#	84.15	43.03	2,459	386,110	71.58	40.98	474	
STS	51,559	86.4	42.32	1,110	386,130	72.95	40.92	765	
	51,567	86.57	42.08	1,058	386,160	72.9	40.7	868	
	51,573	89.2	42.93	37	386,180	71.75	40.37	604	
	51,581	90.23	42.85	399	386,960	66.98	39.7	678	
	51,627	79.23	41.22	1,397	388,120	65.72	38.8	376	
	51,628	80.23	41.17	1,105	388,360	68.83	38.54	785	
	51,633	81.9	41.78	1,230	388,380	68.35	38.05	563	
	51,639	82.78	41.23	982	388,440	69.23	38.25	2,239	
	51,642	84.25	41.78	978	389,270	67.31	37.29	313	

represents the CMA station (ID begins with 5) including the snow water equivalent data. * represents the GSOD station (ID begins with 3) including the snow depth data. NTS, STS and WTS demonstrate the northern slope, southern slope and western part of the TS, respectively.

Space Agency (ESA) Climate Change Initiative (CCI) project (https://www.esa-landcover-cci.org/) and the Global Land Surface Satellite (GLASS) products (https://www.geodata.cn/), respectively, which were used to update the corresponding parameters in the WRF model. The CCI-LC consists of a series of global land cover maps (v2.0.7) at a 300 m spatial resolution from 1992 to 2015 (ESA, 2017). The global overall accuracy of the CCI-LC product exceeds 75.4% (ESA, 2017). The CCI-LC 2015 was converted into the USGS-24 categories as the basis LC in the WRF according to Appendix Table A1 and resampled into a 1 km resolution with the nearest neighbour interpolation. The GLASS LAI generated from the Advanced Very High Resolution Radiometer

(AVHRR) reflectance datasets (Xiao et al., 2016) provides the global 8-day LAI product at a spatial resolution of 0.05° × 0.05° from 1981 to the present. Previous studies demonstrated that the GLASS LAI data have higher quality than the other LAI products (Fang et al., 2019; Xiao et al., 2014). In order to daily update the real-time LAI in WRF for the inner domain, the 8-day GLASS LAI data from 2005 to 2015 have been linearly interpolated to a daily scale at a 9 km resolution via bilinear interpolation.

Table 2
Information of forest stations.

Name	Longitude (°E)	Latitude (°N)	Altitude (m)	Period	Position
TSSAR	84.4	43.27	1776	2005-09-01-2015-08-31	Western Ili Valley
TC	88.12	43.88	1935	2005-09-01-2015-08-31	NTS
BYG	85.98	43.85	1547	2012-09-01-2015-08-31	ETS

2.3. Model configuration

In this study, the snowpack simulations were performed by means of the WRF 4.01 (Skamarock and Klemp, 2008) coupled with the Noah-MP (Niu et al., 2011; Yang et al., 2011) model in the TS from August 2005 to August 2015. The model was initialized at 00:00 UTC on 1st August each year and terminated on 31st August the next year. The initial August output was discarded as a model spin-up (Norris et al., 2018), hence the hydrological year (from September to August) retained output. The model output could include 10 full cold seasons during 2005–2015. The realistic orographic precipitation processes could be revealed better when the resolution is smaller than 10 km (Norris et al., 2015; Wrzesien et al., 2018). The WRF/Noah-MP was configured with the one-way double nested domains, where the outer and inner domains have a spatial resolution of 27 km and 9 km, respectively, with 35 vertical levels from the surface up to 50 hPa (Fig. 1a). The coarse Domain 1 (d01) had 317 × 145 grids in the west-east and south-north direction and the innermost Domain 2 (d02) was nested with 304 × 133 grids. The ERA-Interim dataset has proved to perform very well in Central Asia (Hu et al., 2016, 2014) and has successfully been applied to the regional climate downscaling (Chen et al., 2019; Qiu et al., 2017). Therefore, the ERA-Interim (0.75° × 0.75°) reanalysis data that were updated every 6 h have been chosen as the initial and lateral boundary conditions for two domains (https://www.ecmwf.int/en/forecasts/datasets/reanalysis-datasets/era-interim). The parameterization schemes followed the previous studies (Norris et al., 2017, 2015) and are presented in Table 3: the Single-Moment 6-Class (WSM-6) cloud microphysical scheme (Hong and Lim, 2006), Yonsei University planetary boundary layer (YSU) (Hong et al., 2006), Rapid Radiation Transfer (RRTM) longwave radiation model (Mlawer et al., 1997), Dudhia shortwave radiation model (Dudhia, 1989), MM5 Monin-Obukhov surface layer (Monin and Obukhov, 1959), Kain-Fritsch Cumulus Scheme (Kain, 2004) and Noah-MP Land Surface (Niu et al., 2011).

The land surface physics' scheme has a significant influence on the accuracy of the snow simulation (Liu et al., 2019). As a new generation of the Noah land surface model, the Noah-MP model enhances the physical and multiple parameterization options for the different land–atmosphere interaction processes, which includes a multi-layer snowpack, multiple options for dynamic vegetation phenology, frozen soil and infiltration, groundwater and runoff (Fig. 2) (Niu et al., 2011; Yang et al., 2011). The three-layer snow structure could help to resolve the snowpack internal processes and to estimate the snow processes in a better way compared to the Noah LSM (Niu et al., 2011). Snow density is predicted by taking into account for the destructive metamorphism, melt metamorphism, and compaction due to the weight of the third snow layer and its overlying layers (Anderson, 1976; Sun et al., 1999). In addition, the dynamic vegetation model allows the assimilation of the multi-sources' vegetation dataset, which plays a key role in the

Table 3
Main physical parameterizations used in the numerical simulations.

Simulation period	2005-09-01 to 2015-08-31
Model Version:	Version 4.01
Nest:	2
Horizonal resolution (innermost):	9 km
Number of grids (innermost):	304*133
Vertical Levels:	35
Microphysics' scheme:	WSM-6
Longwave radiation scheme:	RRTM
Shortwave radiation scheme:	Dudhia
Surface layer:	Revised MM5 Monin-Obukhov
Planetary boundary layer:	YSU
Cumulus parameterization:	Kain-Fritsch
Initial/lateral boundary condition:	ERA-Interim
Land surface model:	Noah-MP

snow energy balance and snow interception (Gan et al., 2019). The main parameterization schemes in the Noah-MP are as follows (Niu et al., 2011): the Ball-Berry vegetation stomatal resistance (Ball et al., 1987; Collatz et al., 1992, 1991), Monin-Obukhov surface layer drag coefficient, CLASS (Canadian Land Surface Scheme) ground surface albedo, the Noah soil moisture factor for stomatal resistance, Jordan's scheme for precipitation partitioning between snow and rain (Jordan, 1991), semi-implicit snow/soil temperature time scheme and two streams applied to the vegetated fraction for the radiative transfer option.

2.4. Experimental design

We designed two numerical control experiments so as to study the effect of the vegetation parameters (LC, LAI and FVEG) on the snowpack simulation in the TS (Table 4). Compared with CCI-LC 2015, USGS-LC showed a underestimation in the barren land (−16%), grassland (−4.5%), but a overestimation in shrubland (19.9%), cropland (1.4%) and forest (0.3%). The multi-year averaged LAI from GLASS in d02 exhibited a significant underestimation (−151.43%) than that from the WRF look-up table (Fig. 1f). The CCI-LC 2015 was selected as input land cover data in d02 for the EXP1. In addition, the daily GLASS LAI data and calculated FVEG were updated in d02. The LC, LAI and FVEG have used the default options from the WRF geographical dataset for the outer domain. The default USGS LC data, the monthly LAI and yearly maximum FVEG from the look-up table were carried out in both d01 and d02 for the EXP2. The LAI and FVEG in a cell grid were determined by the percentage of each land use type and its corresponding value.

The calculated FVEG in the Noah-MP for EXP1 could be expressed as:

$$F_{veg} = 1 - e^{(-0.52 \times (LAI + SAI))} \tag{1}$$

where the LAI is the leaf area index and the SAI (equal to 0.1*LAI) stands for the stem area index.

As one of the primary energy of snowmelt, the net longwave radiation ($LW_{a,v}$) in a cell grid in the Noah-MP model can be computed as below (Niu et al., 2011):

$$
\begin{aligned}
LW_{a,v} \\
= F_{veg}\{-\varepsilon_v \cdot [1 + (1 - \varepsilon_v)(1 - \varepsilon_{surf})] \cdot LW_{atm}^{\downarrow} - \varepsilon_v \varepsilon_{surf} \sigma T_{surf}^4 \\
+ [2 - \varepsilon_v(1 - \varepsilon_{surf})] \cdot \varepsilon_v \sigma T_{veg}^4 \}
\end{aligned} \tag{2}
$$

where ε_v and ε_{surf} are the emissivity of vegetation and ground, respectively. σ is the Stefan-Boltzmann constant ($5.67 * 10^{-8} W/m^2 * K^4$).

The emissivity of vegetation in the model is defined as the function of effective leaf area index (ELAI) and effective stem area index (ESAI) after burying by snow (Niu et al., 2011):

$$\varepsilon_v = 1 - e^{-(ELAI + ESAI)/\bar{\mu}} \tag{3}$$

where μ fixed as 1 is the average inverse optical depth for longwave radiation.

The snow cover fraction (f_{snow}) is determined by the snow depth, snow density and ground roughness length (z_0) (Niu and Yang, 2007):

$$f_{snow} = \tanh\left(\frac{h_{snow}}{2.5 z_0 \left(\frac{\rho_{snow}}{\rho_{new}}\right)^m}\right) \tag{4}$$

where ρ_{snow} and ρ_{new} (100 kg m^{-3}) are the bulk and fresh density of snow, respectively. z_0 is equal to 0.01 m. m is the melting factor calibrated against observed f_{snow} or albedo in the melting season, here is 1.0. h_{snow} is the SD, which is directly related to the interception and unload of the vegetation canopy.

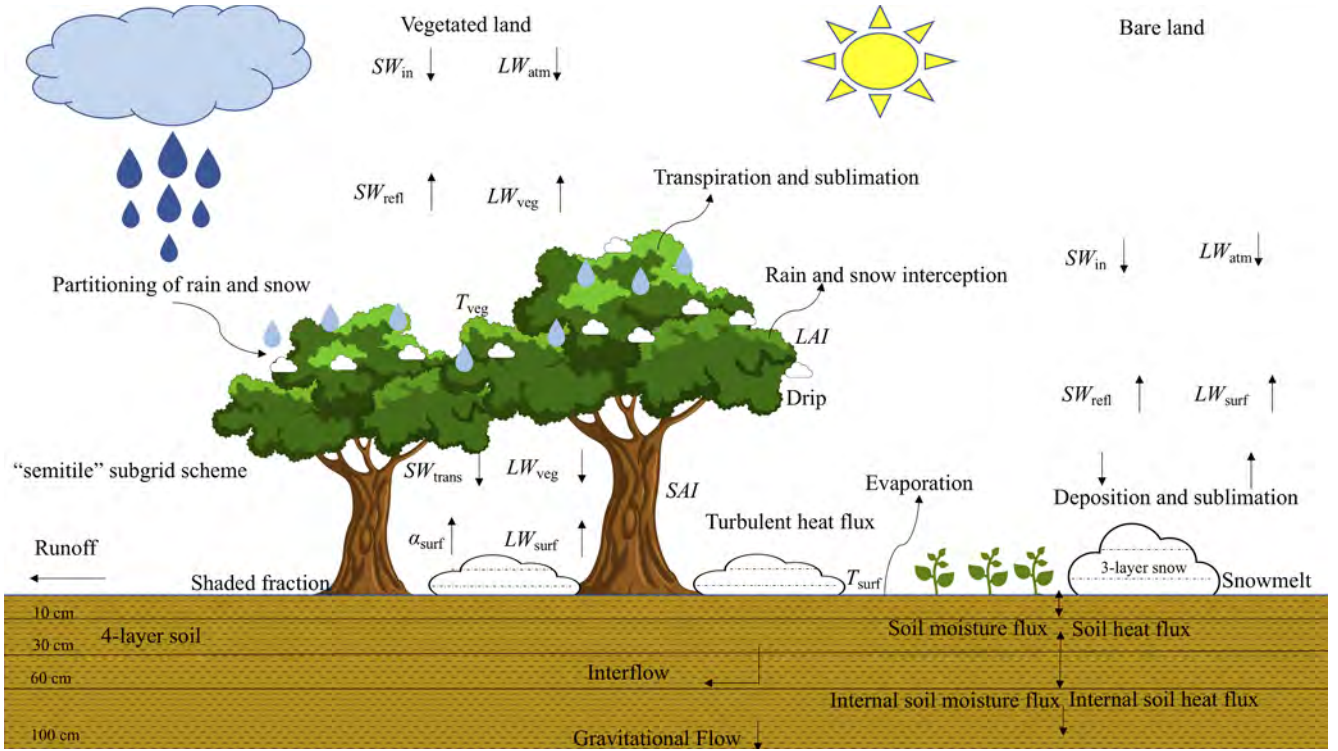The maximum amount of water within vegetation canopy (P_{max}) can be expressed as (Niu and Yang, 2004):

Fig. 2. Schematic diagram for the snow process in the Noah-MP model. SW_{in} represents the incoming shortwave radiation; SW_{refl} represents the reflected shortwave radiation; LW_{atm} represents the atmospheric longwave radiation; LW_{veg} represents the longwave radiation emitted by vegetation; SW_{trans} represents the shortwave radiation transfer computed by a modified two-stream approximation scheme; α_{surf} represents the ground absorptivity; LW_{surf} represents the longwave radiation emitted by ground; T_{surf} and T_{veg} represent the ground and vegetation temperature, respectively.

Table 4
Numerical control experiment in the WRF/Noah-MP model for d02.

	EXP1	EXP2
Land use	CCI_2015	default: USGS
dynamic vegetation option	Dveg = 8: Input GLASS LAI; Calculate FVEG	Dveg = 4 (default): Monthly LAI from look-up table; FVEG = Yearly maximum FVEG

$$\rho_{max} = \rho_{max\,h2o}(Veg_{type}) * (LAI + SAI) \quad (5)$$

where P_{maxh2o} is the maximum intercepted water determined by the each vegetation type (VEG_{type}).

2.5. Evaluation method

The output from the WRF model was assessed by the in-situ data and remote sensed data. The precipitation, near-surface air temperature, SD and SWE values from the nearest grid cells of the WRF model were compared with the in-situ observations on different time scales. The performance of the model with respect to the observations was quantified using the Correlation coefficient (R), Mean bias (MB), Root Mean Square Error (RMSE), and Nash-Sutcliffe efficiency (NSE) coefficient and summarized in a Taylor diagram (Taylor, 2001).

$$R = \frac{\sum_{i=1}^{N}[(Sim(i) - Sim_{mean})(Obs(i) - Obs_{mean})]}{\sqrt{\sum_{i=1}^{N}(Sim(i) - Sim_{mean})^2 \sum_{i=1}^{N}(Obs(i) - Obs_{mean})^2}} \quad (6)$$

$$MB = \frac{1}{N}\sum_{i=1}^{N}(Sim(i) - Obs(i)) \quad (7)$$

$$RMSE = \sqrt{\frac{1}{N}\sum_{i=1}^{N}(Sim(i) - Obs(i))^2} \quad (8)$$

$$NSE = 1 - \frac{\sum_{i=1}^{N}(Obs(i) - Sim(i))^2}{\sum_{i=1}^{N}(Obs(i) - Obs_{mean})^2} \quad (9)$$

where N is the total number of observed or simulated data, $Sim(i)$ and $Obs(i)$ are the simulated and observed values at timestep i, respectively, and Sim_{mean} and Obs_{mean} are the mean of the simulated and observed values, respectively.

3. Results

3.1. Performance of the model simulations

3.1.1. Near-surface air temperature and precipitation

The surface temperature and precipitation determine the snowfall amount. Therefore, we first evaluated the mean daily near-surface air temperature at 2 m (T2) and the total precipitation in the cold season, using the meteorological stations. Overall, the EXP1 showed less bias in precipitation and T2 than the EXP2 did (Table 5). The pattern of MB in T2 and precipitation for the EXP1 and EXP2 was displayed in Fig. 3. Almost all stations demonstrated a consistent cold bias in T2 (Fig. 3a and b). Low cold bias (smaller than −0.8 °C/day) values prevailed in the Ili Valley and the intersection between the Eastern and Northern TS. In contrast, large cold bias values (larger than −1.6 °C/day) were observed in the Western and Central TS, especially in the high-altitude regions where the cold bias exceeded −5 °C/day. The cold bias of T2 was smaller in the NTS than that in the STS and western part (WTS) on

Table 5
The mean bias of the temperature and precipitation averaged from all station in the TS and its sub-regions during the cold season.

	EXPs	TS	NTS	STS	WTS
Daily T2 (°C/day)	EXP1	−2.76	−1.81	−3.89	−2.76
	EXP2	−3.06	−1.86	−3.96	−3.06
Monthly T2 (°C/month)	EXP1	−2.78	−1.83	−3.92	−2.74
	EXP2	−2.93	−1.88	−4.00	−3.07
Precipitation (mm/cold season)	EXP1	−1.65	−4.27	0.64	
	EXP2	−1.68	−4.29	0.63	

the daily and monthly scales (Table 5). Compared with the EXP2, the EXP1 had a smaller cold bias in T2. It was noted that both the EXP1 and EXP2 exhibited a significantly underestimated precipitation in the low-altitude regions (Fig. 3c and 3d), but overestimation was noticed over 20 mm in the high-altitude regions during the cold season. The model had a larger bias spread of precipitation in the NTS than in the STS (Table 5).

3.1.2. SD

The performance of the snow simulation from the EXPs was displayed in Figs. 4–6. Generally, the Taylor diagram demonstrated that the EXP1 slightly improved the performance of SD simulation than the EXP2 did in the TS and its sub-regions on a daily and monthly scales (Fig. 4a). Both the EXP1 (NSE = 0.71) and EXP2 (NSE = 0.68) showed a high accuracy in the SD simulations (Fig. 6a), especially in the Ili Valley and the intersection of the Eastern and Northern TS where the R value exceeded 0.7 (Fig. 5a and b), but a general underestimation existed (Fig. 5e and 5f). In contrast, the model simulations showed a relatively poor performance (NSE = 0.33 and 0.30 for EXP1 and EXP2, respectively) in the STS with a general overestimation. It was noted that larger RMSE and MB values of the SD simulations on a daily scale for the EXP1 and EXP2 were seen in the NTS than that in the STS (Fig. 5c and d). The large (over 5 cm/day) and small (below 2 cm/day) RMSE values prevailed in the NTS and STS, respectively. Additionally, the SD values with low accuracy and large overestimation were seen in the high-altitude regions. Similarly, the RMSE values exceeding 9 cm/day

were found in the high-altitude regions.

3.1.3. SWE and TWS

The SWE measurement is performed once every five days in a few meteorological stations (listed in Table 1) when the daily snow depth is exceeds 5 cm. The daily SWE averaged from all stations was exhibited in Fig. 6b. The EXP1 (NSE = 0.69) performed a higher accuracy in the daily SWE simulation than that the EXP2 (NSE = 0.67) did, but both EXPs exhibited a positive bias (MB: 2.3 and 0.66 mm/day, respectively).

Most meteorological stations are located near the city, which resulted in difficulties to prove the performance of the EXPs in the forest and high-altitude regions. Therefore, the daily SD and 5-day SWE from the TSSAR station, daily SD from TC and BYG station, and GRACE monthly TWS anomaly product were chosen to validate the simulation results (Fig. 4b and c-f). Both the SD and SWE from the EXPs exhibited a good shape with the observations (Fig. 6c-f), but a significant underestimation was seen in the SD and SWE simulation. The Taylor diagram indicated that the daily SD simulation in the forest regions in the EXP1 showed a better performance than that in the EXP2 (Fig. 4b). We compared the TWS from the EXPs to the GRACE TWS so as to investigate the role of the SWE in the TWS budget (Fig. 6g). Compared with GRACE, the EXP1 and EXP2 showed an overestimation in the TWS during the cold season except for 2005/2006 and 2006/2007. Although the MB of the EXP1 was slightly higher than that of the EXP2 in the TWS (Table 6). Overall, the smaller RMSE and larger R and NSE in the TWS demonstrated that the EXP1 showed a better estimation of snow mass during the cold season in the TS.

3.2. Spatial distribution of the SD and SWE

The maximum and monthly mean SD and SWE during the cold season for the EXP1 and EXP2 were shown in Fig. 7. Both the EXP1 and EXP2 showed a similar spatial distribution of the snowpack during the cold season. The maximum SD (Fig. 7a and b) and monthly mean SD (Fig. 7c and 7d) values in the WTS and the high-altitude regions of the Ili Valley exceeded 100 cm and 60 cm, respectively, correspondingly,
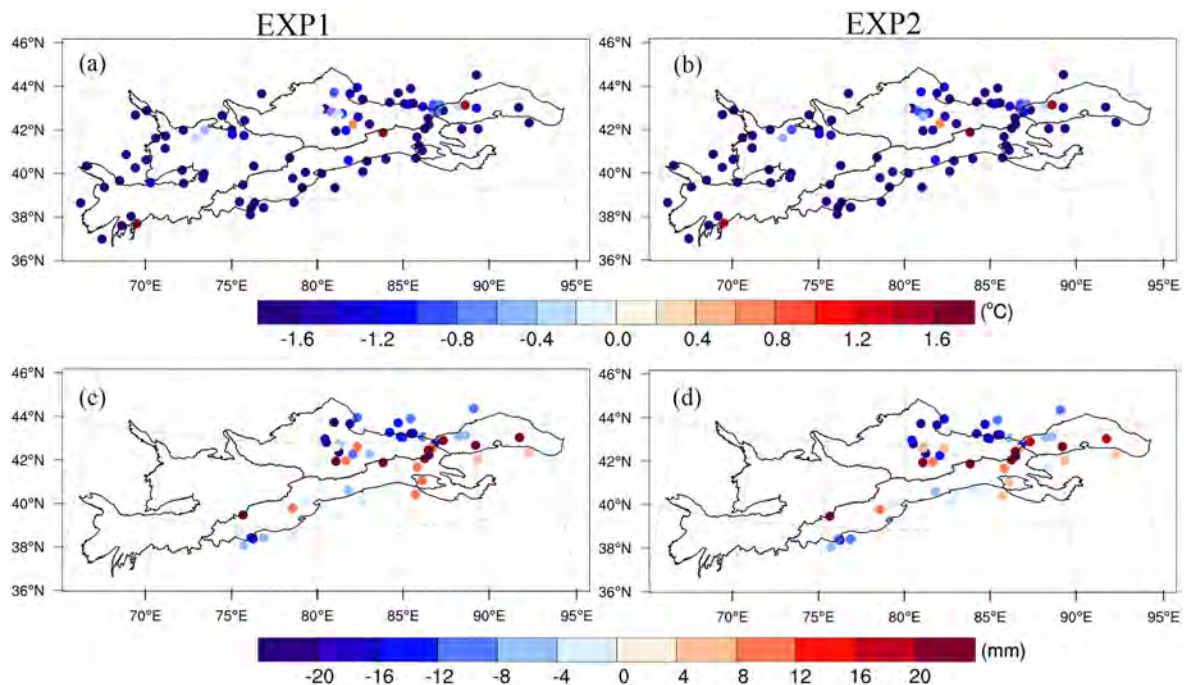
Fig. 3. The mean bias of the daily mean T2 (°C) (a and b) and total precipitation (mm) (c and d) during the cold season between the EXPs and the meteorological observations.
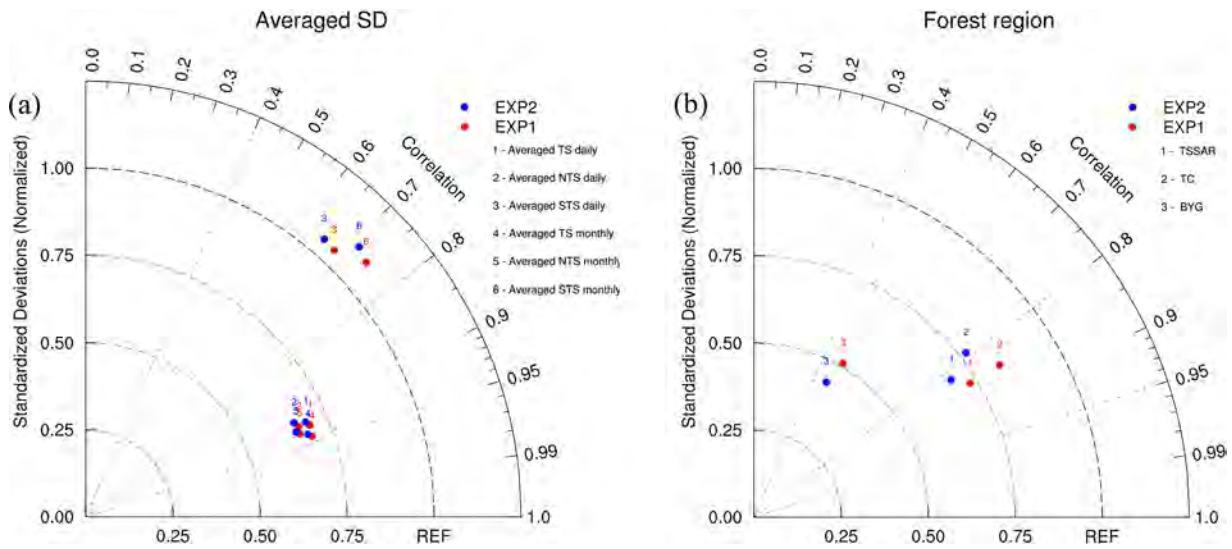
Fig. 4. Taylor diagram comparing in-situ snow depth with WRF simulations. (a) Averaged snow depth from all stations in the TS, NTS, and STS on a daily and monthly time scales, and (b) daily SD at the forest region. Values closer to the reference point indicate a higher correlation and smaller differences in variances.

the peak SWE reached 300 mm (Fig. 7e and f) and 150 mm (Fig. 7g and h). In addition, the values of SD and SWE decreased from north to south, and from west to east.

3.3. Differences of the LAI, FVEG and SWE between the EXP1 and EXP2

In order to examine the impact of vegetation parameters on the snowpack simulation, the differences between the EXP1 and EXP2 in the mean LAI, FVEG, and SWE during the snow accumulation (November-January) and melting (February-March) season were shown
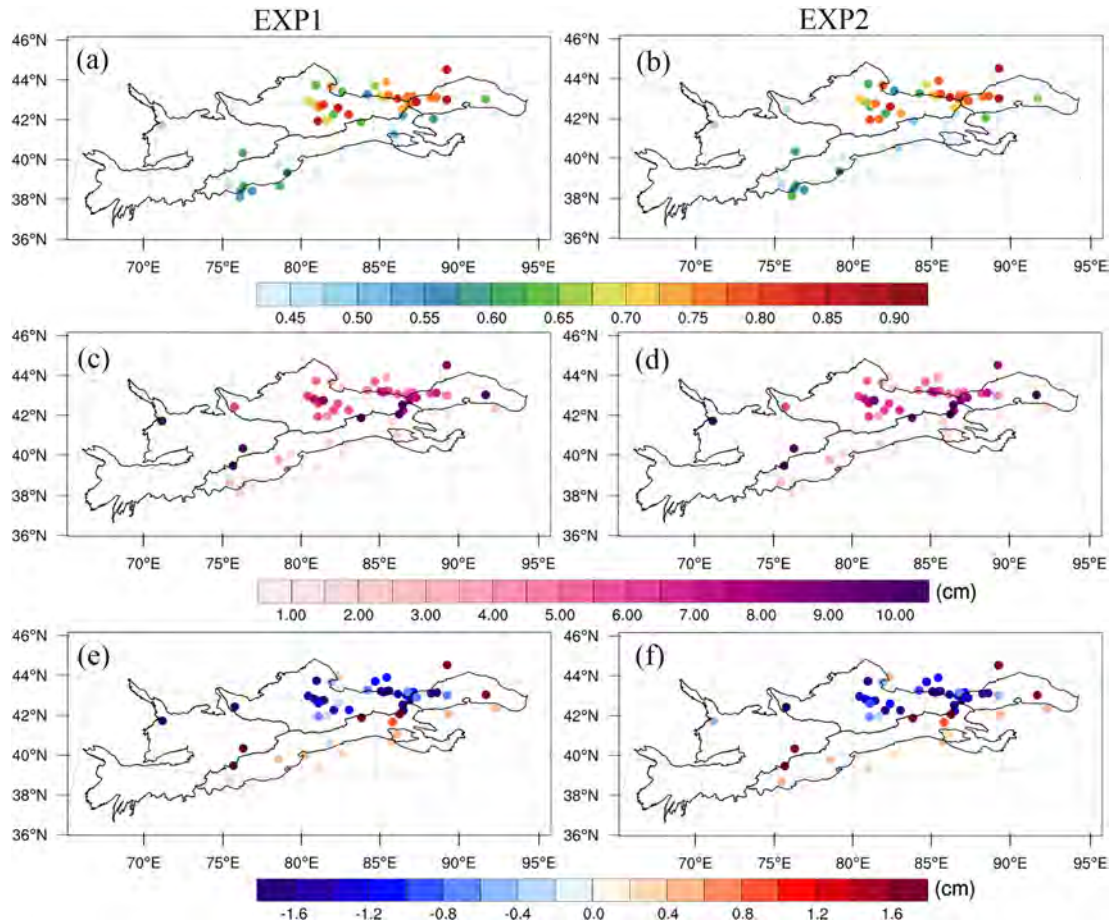

Fig. 5. Spatial distribution of the correlation coefficients (a and b), root-mean-square error (cm/day) (c and d) and mean bias (cm/day) (e and f) between the daily SD from the EXPs and the observed SD.
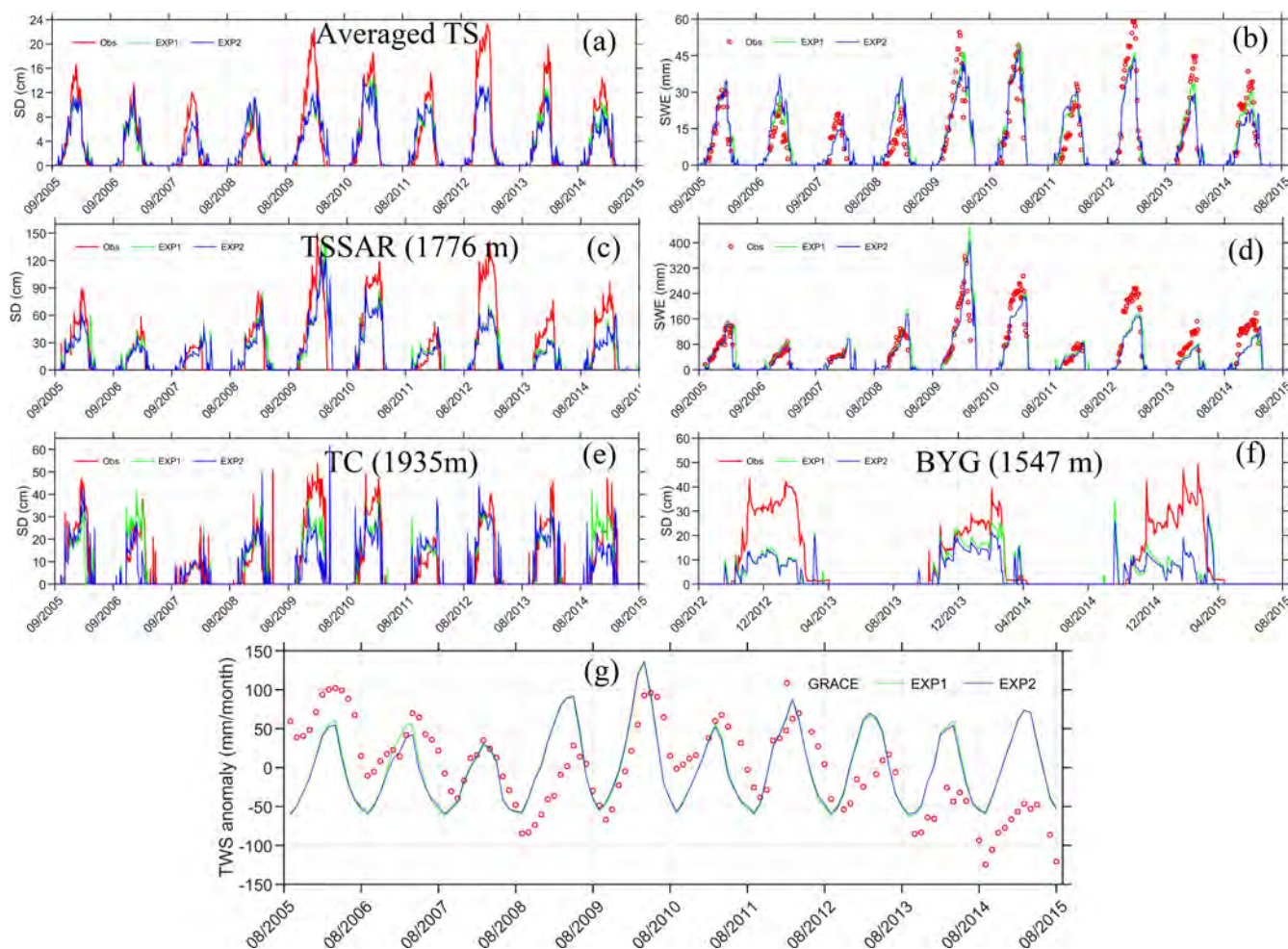
Fig. 6. Comparison of time series observations and simulations of the daily SD (a) and SWE (b) averaged from all station, the daily SD averaged from stations in the NTS (c) and STS (d), the daily SD (e) and SWE (f) at TSSAR station, and the daily SD at TC (g) and BYG (h) station. (j) Comparison of the TWS anomaly between GRACE and the simulations.

Table 6

The correlation coefficient, root-mean-square error (mm/month) and mean bias (mm/month) of the monthly TWS anomaly and GRACE monthly TWS anomaly during the cold season in the TS for the EXP1 and EXP2.

	R	RMSE (mm/month)	MB (mm/month)	NSE
EXP1	0.43**	56.2	0.45	− 0.19
EXP2	0.40**	56.7	0.43	− 0.21

** Significant on the 0.01 level.

in Fig. 8. Both the mean LAI (m^2/m^2) (Fig. 8a and b) and FVEG (%) (Fig. 8c and d) during the snow accumulation and melting season in the EXP1-EXP2 exhibited a consistent underestimation. However, the underestimation of LAI in the snow melted season (−0.017 m^2/m^2/season) was larger than in the snow accumulated season (−0.008 m^2/m^2/season). In addition, highly underestimated values prevailed in the WTS and the high-altitude regions of the Ili Valley. Significantly overestimated values were only sporadically noticed in the low-altitude regions. In contrast, the SWE difference displayed an opposite distribution. Compared with the SWE in the EXP2, the EXP1 demonstrated a significant overestimation during the cold season in the TS (Table 7). These significantly overestimated SWE values were concentrated in the WTS and the high-altitude regions of the Ili Valley (Fig. 8e and 8f). In addition, the magnitude of the overestimation in the melting season (−3.75 mm/season) was larger than that in the accumulation season (−1.94 mm/season).

4. Discussion

4.1. Impact of the vegetation parameters on the snow simulation

The performance of the EXP1 and EXP2 in the TS indicated that accurate vegetation parameters could improve the estimation of the SD and SWE in the WRF/Noah-MP (Fig. 4 and Table 6). It has been reported that a difference in vegetation parameters could cause a significant variability in the snow process through the association with the snow surface energy and snow interception (Kumar et al., 2019; Todt et al., 2019). The impact of the vegetation on the snow mass depends on the vegetation density, climate type and meteorological conditions, which play a significant role in the vegetation temperature, atmospheric shortwave and longwave through the whole snowmelt season (Pomeroy et al., 2009; Sicart et al., 2004). More dense vegetation canopy could increase the intercepted snowfall (Fig. 9c and d). The sublimation could reach up to 50% of the intercepted snowfall and reduce the ground snow mass (Martin et al., 2013; Zheng et al., 2019). Compared with the EXP2, the widely significant underestimation of the LAI and FVEG in the EXP1 (Fig. 8a–d) could enhance the snow surface reflection and reduce the absorption of the solar radiation (Rutter et al., 2009; Webster et al., 2016), which caused a significant albedo increase (Table 7, Fig. 9e and f).

The difference in the monthly mean SWE (Fig. 8e) during the snow accumulation period was mainly caused by the difference in intercepted snowfall (Fig. 9c) and precipitation (Fig. 9a). The overestimation of the
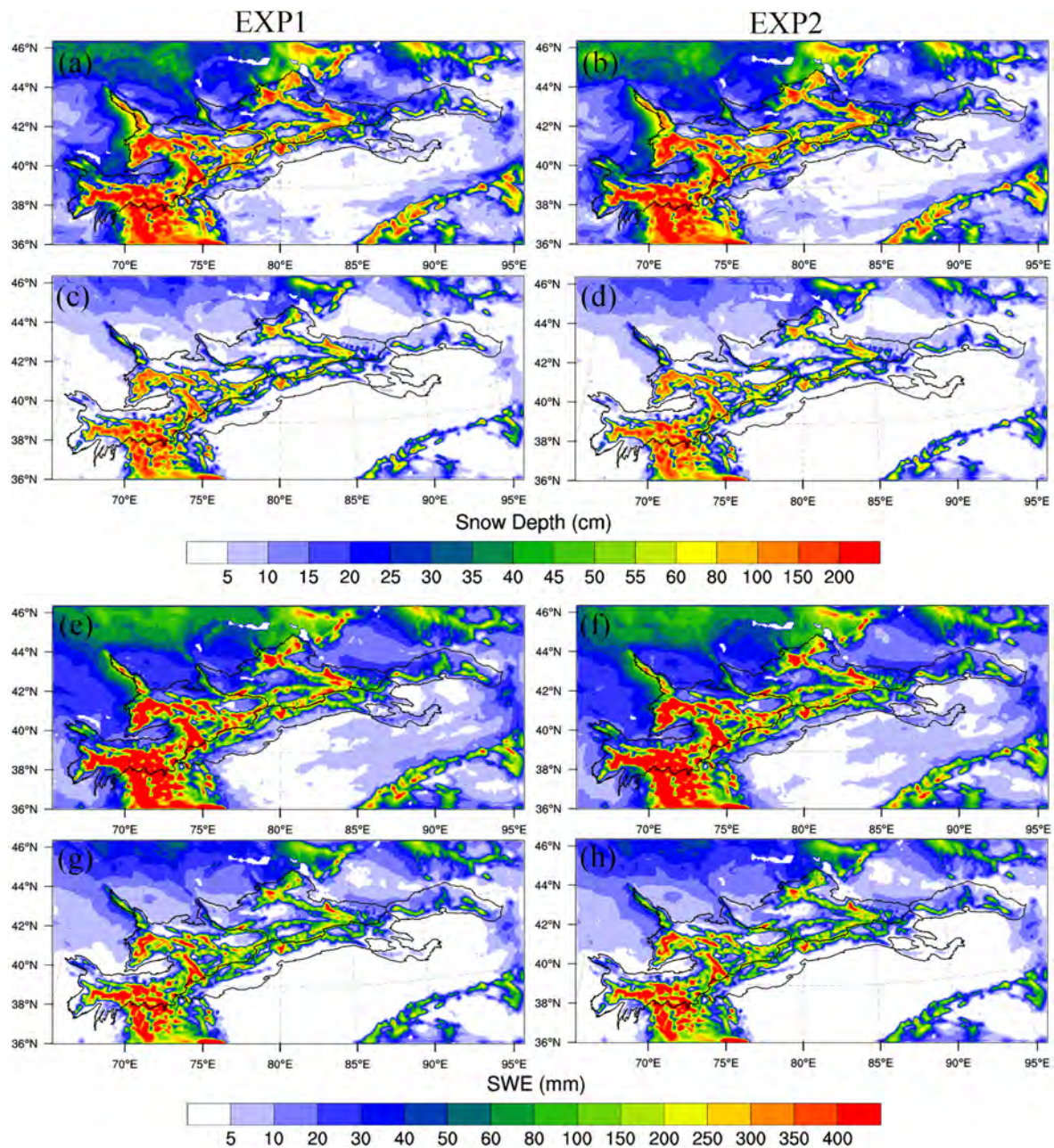
Fig. 7. Climatology (2005–2015) of maximum SD (a and b), monthly mean SD (c and d), peak SWE (e and f), and monthly mean SWE (g and h) in the cold season for the EXP1 and EXP2.

precipitation and more intercepted snowfall during the snow accumulation period indicated more snow in the ground in EXP1 than that in EXP2 (Table 7). More vegetation in the plain of WTS (Fig. 8a) could induce the evapotranspiration enhancement to increase the atmospheric water vapor content, which was beneficial to enhance the cloud cover and increase precipitation in the mountainous regions by the large-scale moisture transport (Piao et al., 2020; Teuling et al., 2017). In addition, the enhanced cloud cover could cause an overestimation of the net longwave radiation (Forsythe et al., 2015; Pritchard et al., 2019), and enhanced the ground heat flux and T2 (Table 7). Meanwhile, turbulent mixing between the snow surface and the vegetation canopy could be suppressed by the dense canopy to act as a sink for cold air (Marks et al., 2008; Varhola et al., 2010), bringing about a lower T2 (Link and Marks, 1999; Webster et al., 2016). The aboved reasons may contribute to the higher T2 in the EXP1 than that in EXP2 during the snow accumulation period (Fig. 9g). However, the temperature was significantly lower than the melting point, indicating that the overestimation of the T2 could not result in significant snowmelt changes (Fig. 9i).

During the snow melting period, the energy of snowmelt under the canopy mainly originates from the longwave radiation emitted from the vegetation canopy due to the vegetation reflection and absorption for the shortwave radiation (Pomeroy et al., 2009; Sicart et al., 2004). The significant underestimation of the LAI indicated a lower vegetation emission in the EXP1 (Eq. (3)). Consequently, a significantly reduced energy release from the vegetation was noticeable and resulted in a small probability of snowmelt during the melting period (Ma et al., 2019). Lower LAI regions, such as the Ili Valley and WTS (Fig. 8a), emitted less longwave radiation to the surface ground and decreased the sensible heat flux (Table 7), which could reduce the net longwave radiation at the surface ground and lead to a lower near-surface temperature (Fig. 9h). In addition, the overestimated precipitation during
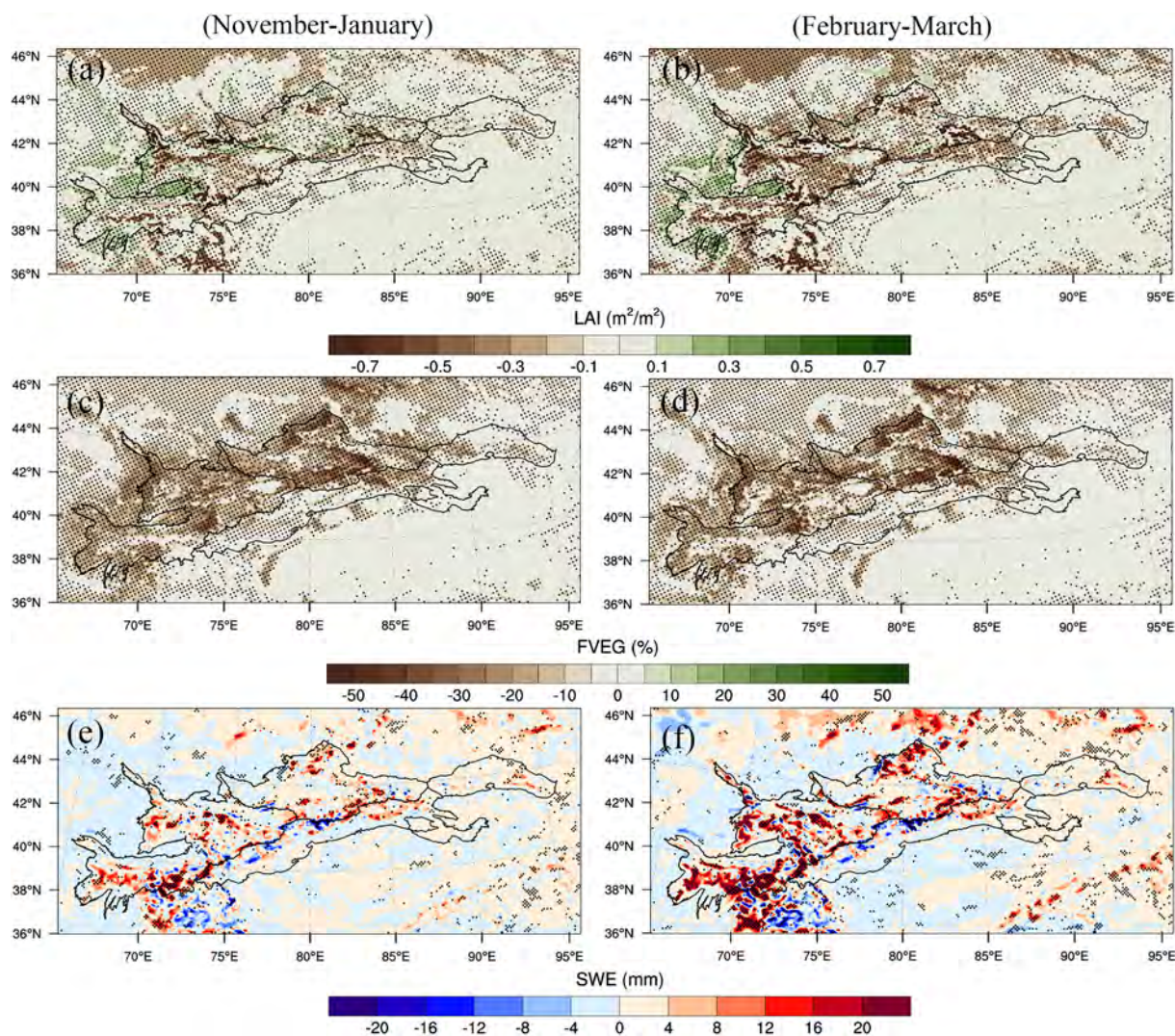
Fig. 8. Differences (EXP1-EXP2) in LAI (a and b), FVEG (c and d) and monthly mean SWE (e and f) between the EXP1 and EXP2 during the cold season (the left side is the snow accumulation season, the right side demonstrates the snow melting season). The black dots in Fig. 8 indicate that the differences are significant (Student's *t*-test: significance level 0.05).

the cold season (Fig. 9a and b) also caused an overestimation of the SWE in both the WTS and high-altitude regions of the Ili Valley during the snow ablation period, which contributed to an increase in reflection of the incoming shortwave radiation and amplified the generally cold bias in the snow ablation period (Pritchard et al., 2019). Consequently, a lower air temperature tended to a low snowmelt rate (Fig. 9h), decreasing the amount of melted snow and maintaining more SWE (Fig. 8f and j), vice versa. Other studies also demonstrated that improving the related vegetation schemes and parameters could better estimate the snow under the canopy environment in the LSMs (Kumar et al., 2019; Ma et al., 2019; Todt et al., 2019). For example, the assimilation of LAI into Noah-MP model contributed to the increase in snow mass by improving the dry bias over the continental United States (Kumar et al., 2019). An improving vegetation emissivity scheme in the Community Land Model (CLM) exhibited a better performance in snow simulation through the stronger longwave radiation and less interception loss in low and medium canopy density regions (Ma et al., 2019). Additionally, the corrected sub-canopy in the longwave radiation scheme in the CLM could reduce the sub-canopy longwave radiation and delay the snowmelt in the Northern Hemisphere (Todt et al., 2019). The diverse canopy structure descriptions in the Flexible Snow Model (FSM2) could capture the small-scale forest snow pattern and prevent overly rapid snowmelt during the melting season (Mazzotti et al., 2020).

4.2. Limitations of the model and forcing data

An accurate estimation of the solid precipitation directly decides on the accuracy of the SD and SWE (Jennings et al., 2018). In the most LSMs and hydrological models, the near-surface air temperature threshold method has been widely applied to distinguish the snowfall and rainfall from the precipitation, but it brings about underestimated snowfall in the dry regions (Li et al., 2018a; Wang et al., 2019). In addition, the accuracy of the forcing data plays a significant role in precipitation and temperature simualtions (Ma et al., 2019). Compared with the meteorological observations, the WRF exhibited a significant overestimation and underestimation in the precipitation at the high and low-altitude regions, respectively, and with a general cold bias in temperature (Fig. 3). Since the inherent performance of the forcing data and the underestimation of measured precipitation from the meteorological observations, the overestimated precipitation in the alpine region may be aggravated (Bonekamp et al., 2018). The snowdrift, snow sublimation and undercatch of snowfall in the pluviometer may contribute to the overestimated precipitation in high-altitude regions during the cold season (Liu et al., 2018; Ye et al., 2005). Moreover, previous studies indicated that the precipitation of ERA-Interim had a significant overestimation in the mountainous area with a widely cold bias (Hu et al., 2016, 2014; Liu et al., 2018). The results of the WRF

Table 7
Differences of the LAI, FVEG, surface climate and energy balance parameters between the EXP1 and EXP2 during the cold season.

Variables	Accumulation season (November-January)	Melting season (February-March)
LAI (m^2/m^2)	−0.08**	−0.17**
FVEG (%)	−13.39**	−12.94**
Ground surface albedo (%)	2.41**	2.37**
Downward longwave radiation (W/m^2)	0.32	−1.16**
Outgoing longwave radiation (W/m^2)	−0.28	−0.05
Downward shortwave radiation (W/m^2)	−0.24	0.56**
Ground heat flux (W/m^2)	0.09*	−0.14
Latent heat flux (W/m^2)	−0.02	−0.11
Sensible heat flux (W/m^2)	−2.31**	−3.53**
Net longwave radiation (W/m^2)	0.08	0.45**
Ground temperature (°C)	0.04**	−0.16
T2 (°C)	0.14	−0.09
Melted snow (mm)	−0.09	−1.29**
Canopy water (mm)	−0.09**	−0.06**
Mean SWE (mm)	1.94**	3.75*
Precipitation (mm)	2.55	−0.12

** and * represent significant values on the 0.05 and 0.1 level, respectively (Student's *t*-test). Net longwave radiation is defined as the surface ground positive towards the atmosphere.

downscaling demonstrated a similar pattern in the TS using the ERA-Interim dataset as forcing data (Chen et al., 2019; Qiu et al., 2017). The solid precipitation is highly sensitive to the cloud microphysics on a complex terrain (Liu et al., 2011). The relatively sophisticated cloud microphysics' scheme, such as the Thompson microphysics' scheme, exhibited a relatively high performance in snowfall simulation in the mountainous area (Fernández-González et al., 2015; Norris et al., 2015). The WSM6 microphysics' scheme could save computing resources, but also resulted in a large uncertainty in snowfall estimation (Yu, 2013). Additionally, the higher spatial resolution could contribute to a more plausible amount and pattern of precipitation in the mountainous area (Bonekamp et al., 2018), but the EXPs with a 9 km resolution has a limited ability to capture the feature of precipitation in the micro-scale regions, especially in the alpine area.

The snow simulation in the Noah-MP is also highly sensitive to the parameterization schemes, especially in the snow melting period (You et al., 2020b). The fresh snow density in the WRF/Noah-MP was much higher than that observed in the TS (minimum 40 kg/m^3) (Chen et al., 2011). The overestimation of fresh snow density and underestimation of precipitation could underestimate SD in the low-altitude regions of the TS (Fig. 5e and 5f). The land data assimilation system and global reanalyses' product almost showed a consistent underestimation of the SWE due to the predicted larger melting of the SWE at nearly freezing temperatures (Broxton et al., 2016). However, the overestimated precipitation and the cold bias caused generally overestimated SWE in the high-altitude TS regions. This was coherent with the performance of the global SWE product in high mountain Asia (Bian et al., 2019).

4.3. Uncertainties and future research

The LC type determined the vegetation parameters in the default options of the WRF/Noah-MP, significantly affecting the land surface energy exchange and precipitation (Cao et al., 2019; Woldemichael et al., 2012). Although the EXP1 updated LC, the conversion from the CCI-LC into the USGS-LC category also brought uncertainty in climate simulation due to the mapping error of the different classification strategies and methods, interpolation, and user criteria (Di Vittorio et al., 2018; Gómez et al., 2016). The generally underestimated LAI in the arid and semi-arid areas during the cold season might affect the

snow accumulation and ablation in the LSMs (Fang et al., 2019; Wang et al., 2016). In addition, the measured errors of in-situ observation due to the constant human disruption such as urban encroachment, sensor upgrade, and station relocation could lead to the bias in model evaluation (Feng et al., 2004; Fiebrich et al., 2010). A point-scale in-situ observation could not fully represent the characteristics of snowpack dynamic compared with a gird from simulations (81 km^2), especially in complex topography, due to spatial heterogeneity (Kumar et al., 2019). The GRACE TWS product was used to evaluate the TWS anomalies caused by the snow accumulation or ablation in the TS, and the TWS from the EXP1 and EXP2 demonstrated a slight overestimation (Fig. 6g and Table 6). However, the TWS anomalies during the cold season did not represent all changes in SWE, because the variations of water mass in soil, glacier, groundwater, lakes and reservoirs were also included in the GRACE measurements (Wrzesien et al., 2018). Moreover, the accuracy of GRACE is also influenced by the gain factors and spatial resolution (Landerer and Swenson, 2012). It is noted that the performance of the WRF/Noah-MP exhibited a big uncertainty in the high-altitude regions and WTS where the lack of sufficient meteorological observations resulted in difficulties to assess the snow simulation.

Since previous studies illustrated that the light-absorbing impurities, such as dust and black carbon deposit on the snowpack, increased the absorption of the shortwave radiation and enhanced the snowmelt rate (Skiles et al., 2018; Zhang et al., 2018). Most RCM LSMs neglect this process, which might cause overestimated SWE and a cold bias, particularly in the high-altitude areas. The role of wind compaction and blowing snow also should be considered in the RCM LSMs, which could cause the large snow density and redistribution of snowpack (Fang and Pomeroy, 2009; Jafarov et al., 2014). The accurate forcing data could reduce the bias in snow simulation in the RCM LSMs (Liu et al., 2019; Terzago et al., 2020), but the WRF model downscaling with the ERA-Interim data has a large deviation in this study (Fig. 5). Recently, representing the new generation of the ERA-Interim reanalysis dataset, the ERA5 has proven to reduce the bias of precipitation and temperature and shows more potential for hydrological applications (Albergel et al., 2018; Nogueira, 2020). Additionally, both the integration of remote sensing albedo products and a more advanced albedo scheme could be applied to decrease the cold bias and improve the performance of the snow process in the LSMs (Kumar et al., 2020; Meng et al., 2018; Wang et al., 2020). Therefore, further research is also required to consider the ERA5 as the initial and lateral boundary conditions and to assimilate the real-time albedo product for the WRF/Noah-MP.

5. Conclusions

This study investigated the impact of the vegetation parameters on the snow simulation in the Tianshan Mountains from 2005 to 2015 through real-time updated remotely sensed leaf area index, green vegetation fraction, and land cover products in the WRF/Noah-MP. Two experiments were conducted including EXP1 with the updated real-time remote sensed data and EXP2 with the default parameter data from the WRF/Noah-MP. Main findings of the study include the following :

1. The peak snow depth (over 100 cm) and snow water equivalent (over 300 mm) values were observed in the Western Tianshan Mountains and high-altitude regions of the Ili Valley. In addition, the snow mass values were significantly larger in the northern slope than that in the southern slope, and the values in western part were larger than that in the eastern part.
2. Both the snow depth and snow water equivalent of the EXP1 and EXP2 showed a general underestimation in the low-altitude regions of the northern slope of the Tianshan Mountains, but an overestimation was found in the high-altitude regions.
3. More realistic vegetation parameters could improve the performance of the snow simulation, especially in the forest regions. The
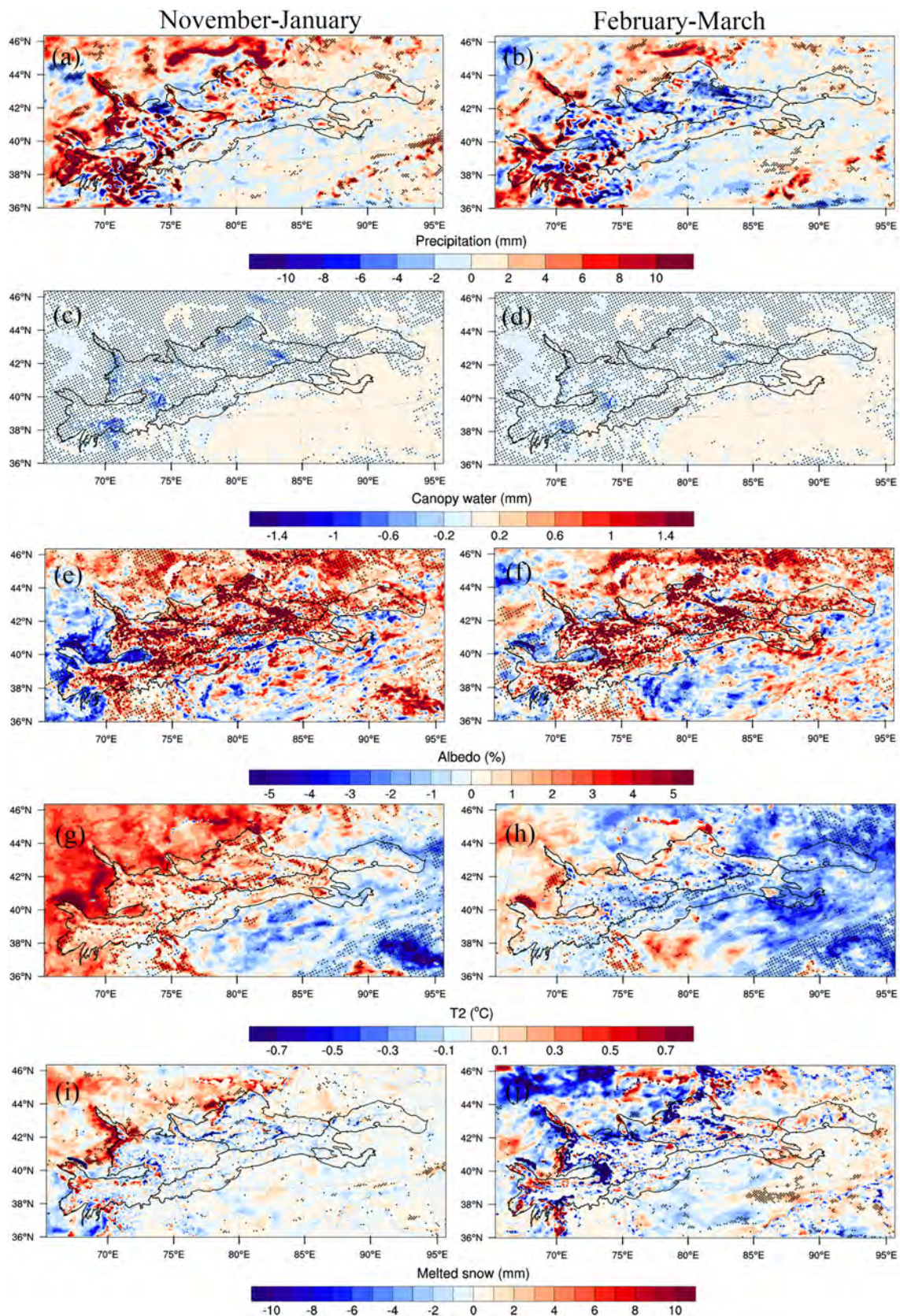
Fig. 9. Differences (EXP1-EXP2) in precipitation (a and b), canopy water (c and d), ground surface albedo (e and f), T2 (g and h) and melted snow (i and j) between the EXP1 and EXP2 during the cold season (the left side shows the snow accumulation season, the right side represents the snow melting season). The black dots in Fig. 9 indicate that the differences are significant (Student's *t*-test: significance level 0.05).

integrated remote sensing vegetation parameter products caused an increased albedo and less snow interception, particularly in the snow ablation period, and less vegetation density could reduce the longwave radiation emitted from the canopy at the surface, causing the lower near-surface temperature and slower snowmelt rate. Less intercepted snowfall and melted snow contributed to more snow mass on the ground, such as in the Western Tianshan Mountains and the high-altitude regions of the Ili Valley.

CRediT authorship contribution statement

Tao Yang: Conceptualization, Methodology, Software, Writing - original draft. **Qian Li:** Software, Writing - original draft. **Xi Chen:** Conceptualization, Resources. **Rafiq Hamdi:** . **Philippe De Maeyer:** Resources. **Alishir Kurban:** Resources. **Lanhai Li:** Project administration, Conceptualization.

Appendix

Declaration of Competing Interest

The authors declare that they have no known competing financial interests or personal relationships that could have appeared to influence the work reported in this paper.

Acknowledgements

Table A1

Assignment of the CCI-LC categories to the consolidated USGS land cover categories.

Land Use Category	Land Use Description	CCI-LC	Name
1	Urban and Built-up Land	190	Impervious surface
2	Dryland Cropland and Pasture	10, 11, 12,	Cropland, rainfed; Herbaceous cover; Tree or shrub cover
3	Irrigated Cropland and Pasture	20	Cropland, irrigated or post-flooding
4	Mixed Dryland/Irrigated Cropland and Pasture		
5	Cropland/Grassland Mosaic	30, 40	Mosaic cropland (> 50%)/natural vegetation; natural vegetation (< 50%); Mosaic natural vegetation (> 50%)/cropland (< 50%)
6	Cropland/Woodland Mosaic		
7	Grassland	130	Grassland
8	Shrubland	120, 121, 122	Shrubland; Evergreen shrubland; Deciduous shrubland
9	Mixed Shrubland/ Grassland	110	Mosaic herbaceous cover (> 50%)/tree and shrub (< 50%)
10	Savanna		
11	Deciduous Broad leaf Forest	60, 61, 62	Tree cover, broad leaves, deciduous, closed to open (> 15%); Tree cover, broad leaves, deciduous, closed (> 40%); Tree cover, broad leaves, deciduous, open (15-40%)
12	Deciduous Needle leaf Forest	80, 81, 82	Tree cover, needle leaves, deciduous, closed to open (> 15%); Tree cover, needle leaves, deciduous, closed (> 40%); Tree cover, needle leaves, deciduous, open (15-40%)
13	Evergreen Broad leaf	50	Tree cover, broad leaves, evergreen, closed to open (> 15%)
14	Evergreen Needle leaf	70, 71, 72	Tree cover, needle leaves, evergreen, closed to open (> 15%); Tree cover, needle leaves, evergreen, closed (> 40%); Tree cover, needle leaves, evergreen, open (15-40%)
15	Mixed Forest	90, 100	Tree cover, mixed leaf type (broad and needle leaves); Mosaic tree and shrub (> 50%)/herbaceous cover (< 50%)
16	Water Bodies	210	Water bodies
17	Herbaceous Wetland	180	Shrub or herbaceous cover, flooded, fresh/saline/brakish water
18	Wooden Wetland	160, 170	Tree cover, flooded, fresh or brakish water; Tree cover, flooded, saline water
19	Barren or Sparsely Vegetated	150, 151, 152, 153, 200, 201, 202	Sparse vegetation (tree, shrub, herbaceous cover) (< 15%); tree cover (< 15%)Sparse shrub (< 15%); Sparse herbaceous cover (< 15%); Bare areas; Consolidated bare areas; Unconsolidated bare areas
20	Herbaceous Tundra		
21	Wooded Tundra		
22	Mixed Tundra		
23	Bare Ground Tundra	140	Lichens and mosses
24	Snow or Ice	220	Permanent snow and ice

References

Anderson, Eric, A., 1976. A point energy and mass balance model of a snow cover. Vol. 19. US Department of Commerce, National Oceanic and Atmospheric Administration, National Weather Service, Office of Hydrology, 1976.

Aizen, V.B., Aizen, E.M., Melack, J.M., Dozier, J., 1997. Climatic and hydrologic changes in the Tien Shan, central Asia. J. Clim. 10, 1393–1404. https://doi.org/10.1175/1520-0442(1997)010<1393:CAHCIT>2.0.CO;2.

Albergel, C., Dutra, E., Munier, S., Calvet, J.C., Munoz-Sabater, J., De Rosnay, P., Balsamo, G., 2018. ERA-5 and ERA-Interim driven ISBA land surface model simulations: which one performs better? Hydrol. Earth Syst. Sci. 22, 3515–3532. https://doi.org/10.5194/hess-22-3515-2018.

Alonso-González, E., Ignacio López-Moreno, J., Gascoin, S., García-Valdecasas Ojeda, M., Sanmiguel-Vallelado, A., Navarro-Serrano, F., Revuelto, J., Ceballos, A., Esteban-Parra, M.J., Essery, R., 2018. Daily gridded datasets of snow depth and snow water equivalent for the Iberian Peninsula from 1980 to 2014. Earth Syst. Sci. Data 10, 303–315. https://doi.org/10.5194/essd-10-303-2018.

Bair, E.H., Rittger, K., Skiles, S.M.K., Dozier, J., 2019. An examination of snow albedo estimates from MODIS and their impact on snow water equivalent reconstruction. Water Resour. Res. 55, 7826–7842. https://doi.org/10.1029/2019WR024810.

Ball, J.T., Woodrow, I.E., Berry, J.A., 1987. A model predicting stomatal conductance and its contribution to the control of photosynthesis under different environmental conditions. In: Progress in Photosynthesis Research. Springer, Dordrecht, pp. 221–224.

Ballesteros-Cánovas, J.A., Trappmann, D., Madrigal-González, J., Eckert, N., Stoffel, M., 2018. Climate warming enhances snow avalanche risk in the Western Himalayas. Proc. Natl. Acad. Sci. U. S. A. 115, 3410–3415. https://doi.org/10.1073/pnas.1716913115.

Barnett, T.P., Adam, J.C., Lettenmaier, D.P., 2005. Potential impacts of a warming climate on water availability in snow-dominated regions. Nature 438, 303–309. https://doi.org/10.1038/nature04141.

Bian, Q., Xu, Z., Zhao, L., Zhang, Y.F., Zheng, H., Shi, C., Zhang, S., Xie, C., 2019. Evaluation and intercomparison of multiple snow water equivalent products over the tibetan plateau. J. Hydrometeorol. 20, 2043–2055. https://doi.org/10.1175/JHM-D-19-0011.1.

Bonekamp, P.N.J., Collier, E., Immerzeel, W., 2018. The Impact of spatial resolution, land use, and spinup time on resolving spatial precipitation patterns in the Himalayas. J. Hydrometeorol. 19, 1565–1581. https://doi.org/10.1175/JHM-D-17-0212.1.

Brown, R.D., Mote, P.W., 2009. The response of Northern Hemisphere snow cover to a changing climate. J. Clim. 22, 2124–2145. https://doi.org/10.1175/2008JCLI2665.1.

Broxton, P.D., van Leeuwen, W.J.D., Biederman, J.A., 2019. Improving snow water equivalent maps with machine learning of snow survey and lidar measurements. Water Resour. Res. 55, 3739–3757. https://doi.org/10.1029/2018WR024146.

Broxton, P.D., Zeng, X., Dawson, N., 2016. Why do global reanalyses and land data assimilation products underestimate snow water equivalent? J. Hydrometeorol. 17, 2743–2761. https://doi.org/10.1175/JHM-D-16-0056.1.

Cao, Q., Wu, J., Yu, D., Wang, W., 2019. The biophysical effects of the vegetation restoration program on regional climate metrics in the Loess Plateau, China. Agric. For. Meteorol. 268, 169–180. https://doi.org/10.1016/j.agrformet.2019.01.022.

Chen, F., Barlage, M., Tewari, M., Rasmussen, R., Jin, J., Lettenmaier, D., Livneh, B., Lin, C., Miguez-macho, G., Niu, G., Wen, L., Yang, Z., 2014. Modeling seasonal snowpack evolution in the complex terrain and forested Colorado Headwaters region: A model intercomparison study. J. Geophys. Res. Atmos. 119, 795–819. https://doi.org/10.1002/2014JD022167.Received.

Chen, S., Hamdi, R., Ochege, F.U., Du, H., Chen, X., Yang, W., Zhang, C., 2019. Added value of a dynamical downscaling approach for simulating precipitation and temperature over tianshan mountains area, Central Asia. J. Geophys. Res. Atmos. 124, 11051–11069. https://doi.org/10.1029/2019JD031016.

Chen, X., Wei, W., Liu, M., 2011. Change in fresh snow density in Tianshan Mountains. China. Chinese Geogr. Sci. 21, 36–47. https://doi.org/10.1007/s11769-010-0434-0.

Chen, Y., Li, W., Deng, H., Fang, G., Li, Z., 2016. Changes in central asia's water tower: past, present and future. Sci. Rep. 6, 1–12. https://doi.org/10.1038/srep35458.

Chen, Y., Li, Z., Fang, G., Li, W., 2018. Large hydrological processes changes in the transboundary rivers of Central Asia. J. Geophys. Res. Atmos. 123, 5059–5069. https://doi.org/10.1029/2017JD028184.

Collatz, G., Ribas-Carbo, M., Berry, J., 1992. Coupled photosynthesis-stomatal conductance model for leaves of C4 plants. Funct. Plant Biol. 19, 519. https://doi.org/10.1071/pp9920519.

Collatz, G.J., Ball, J.T., Grivet, C., Berry, J.A., 1991. Physiological and environmental regulation of stomatal conductance, photosynthesis and transpiration: a model that includes a laminar boundary layer. Agric. For. Meteorol. 54, 107–136. https://doi.org/10.1016/0168-1923(91)90002-8.

Corporation, A.I., Corporation, A.I., Division, E.S., 2018. Parameter sensitivity of the Noah-MP land surface model with dynamic vegetation. J. Hydrometeorol. 19, 815–830. https://doi.org/10.1175/JHM-D-17-0205.1.

Dai, L., Che, T., Ding, Y., Hao, X., 2017. Evaluation of snow cover and snow depth on the Qinghai-Tibetan Plateau derived from passive microwave remote sensing. Cryosph 11, 1933–1948. https://doi.org/10.5194/tc-11-1933-2017.

DeWalle, D.R., Rango, A., 2008. Principles of Snow Hydrology. Cambridge University Press.

Di Vittorio, A.V., Mao, J., Shi, X., Chini, L., Hurtt, G., Collins, W.D., 2018. Quantifying the effects of historical land cover conversion uncertainty on global carbon and climate estimates. Geophys. Res. Lett. 45, 974–982. https://doi.org/10.1002/2017GL075124.

Dong, C., 2018. Remote sensing, hydrological modeling and in situ observations in snow cover research: a review. J. Hydrol. 561, 573–583. https://doi.org/10.1016/j.jhydrol.2018.04.027.

Dudhia, J., 1989. Numerical study of convection observed during the winter monsoon experiment using a mesoscale two-dimensional model. J. Atmos. Sci. https://doi.org/10.1175/1520-0469(1989)046<3077:NSOCOD>2.0.CO;2.

ESA. Land Cover CCI Product User Guide Version 2. Tech. Rep. (2017). Available at: maps.elie.ucl.ac.be/CCI/viewer/download/ESACCI-LC-Ph2-PUGv2_2.0.pdf.

Essery, R., 2013. Large-scale simulations of snow albedo masking by forests. Geophys. Res. Lett. 40, 5521–5525. https://doi.org/10.1002/grl.51008.

Essery, R., Rutter, N., Pomeroy, J., Baxter, R., Stähli, M., Gustafsson, D., Barr, A., Bartlett, P., Elder, K., 2009. An evaluation of forest snow process simulations. Bull. Am. Meteorol. Soc. 90, 1120–1136. https://doi.org/10.1175/2009BAMS2629.1.

Fang, X., Pomeroy, J.W., 2009. Modelling blowing snow redistribution to prairie wetlands. Hydrol. Process. 23, 2557–2569. https://doi.org/10.1002/hyp.

Fang, H., Baret, F., Plummer, S., Schaepman-Strub, G., 2019. An overview of global leaf area index (LAI): methods, products, validation, and applications. Rev. Geophys. 57, 739–799. https://doi.org/10.1029/2018RG000608.

Farinotti, D., Longuevergne, L., Moholdt, G., Duethmann, D., Mölg, T., Bolch, T., Vorogushyn, S., Güntner, A., 2015. Substantial glacier mass loss in the Tien Shan over the past 50 years. Nat. Geosci. 8, 716–722. https://doi.org/10.1038/ngeo2513.

Fao/Iiasa/Isric/Isscas/Jrc. "Harmonized world soil database (version 1.2)." FAO, Rome, Italy and IIASA, Laxenburg, Austria (2012).

Feng, S., Hu, Q., Qian, W., 2004. Quality control of daily meteorological data in China, 1951–2000: A new dataset. Int. J. Climatol. 24, 853–870. https://doi.org/10.1002/joc.1047.

Fernández-González, S., Valero, F., Sánchez, J.L., Gascón, E., López, L., García-Ortega, E., Merino, A., 2015. Numerical simulations of snowfall events: sensitivity analysis of physical parameterizations. J. Geophys. Res. 120, 10130–10148. https://doi.org/10.1002/2015JD023793.

Fiebrich, C.A., Morgan, Y.R., Mccombs, A.G., Hall, P.K., Mcpherson, R.A., 2010. Quality assurance procedures for mesoscale meteorological data. J. Atmos. Ocean. Technol. 27, 1565–1582. https://doi.org/10.1175/2010JTECHA1433.1.

Forsythe, N., Hardy, A.J., Fowler, H.J., Blenkinsop, S., Kilsby, C.G., Archer, D.R., Hashmi, M.Z., 2015. A detailed cloud fraction climatology of the upper indus basin and its implications for near-surface air temperature. J. Clim. 28, 3537–3556. https://doi.org/10.1175/JCLI-D-14-00505.1.

Gan, Y., Liang, X.Z., Duan, Q., Chen, F., Li, J., Zhang, Y., 2019. Assessment and reduction of the physical parameterization uncertainty for noah-MP land surface model. Water Resour. Res. 55, 5518–5538. https://doi.org/10.1029/2019WR024814.

Ge, J., Pitman, A.J., Guo, W., Zan, B., Fu, C., 2020. Impact of revegetation of the Loess Plateau of China on the regional growing season water balance. Hydrol. Earth Syst. Sci. 24, 515–533. https://doi.org/10.5194/hess-24-515-2020.

Gómez, C., White, J.C., Wulder, M.A., 2016. Optical remotely sensed time series data for land cover classification: A review. ISPRS J. Photogramm. Remote Sens. 116, 55–72. https://doi.org/10.1016/j.isprsjprs.2016.03.008.

Gou, J., Wang, F., Jin, K., Mu, X., Chen, D., 2019. More realistic land-use and vegetation parameters in a regional climate model reduce model biases over China. Int. J. Climatol. 4825–4837. https://doi.org/10.1002/joc.6110.

Guo, L., Li, L., 2015. Variation of the proportion of precipitation occurring as snow in the Tian Shan Mountains. China. Int. J. Climatol. 35, 1379–1393. https://doi.org/10.1002/joc.4063.

Hall, D.K., Riggs, G.A., Foster, J.L., Kumar, S.V., 2010. Development and evaluation of a cloud-gap-filled MODIS daily snow-cover product. Remote Sens. Environ. 114, 496–503. https://doi.org/10.1016/j.rse.2009.10.007.

Hedstrom, N.R., Pomeroy, J.W., 1998. Measurements and modelling of snow interception in the boreal forest. Hydrol. Process. 12, 1611–1625. https://doi.org/10.1002/(SICI)1099-1085(199808/09)12:10/11<1611::AID-HYP684>3.0.CO;2-4.

Helbig, N., Moeser, D., Teich, M., Vincent, L., Lejeune, Y., Sicart, J.-E., Monnet, J.-M., 2019. Snow processes in mountain forests: Interception modeling for coarse-scale applications. Hydrol. Earth Syst. Sci. Discuss. 1–24. https://doi.org/10.5194/hess-2019-348.

Hong, S., Lim, J., 2006. The WRF Single-Moment 6-Class Microphysics Scheme (WSM6). J. Korean Meteorol, Soc.

Hong, S.Y., Noh, Y., Dudhia, J., 2006. A new vertical diffusion package with an explicit treatment of entrainment processes. Mon. Weather Rev. 134, 2318–2341. https://doi.org/10.1175/MWR3199.1.

Hu, Z., Qi, H.u., Zhang, C., Chen, X., Li, Q., 2016. Evaluation of reanalysis, spatially interpolated and satellite remotely sensed precipitation data sets in central Asia. J. Geophys. Res. Atmos. 121, 5648–5663. https://doi.org/10.1002/2016JD024781.Received.

Hu, Z., Zhang, C., Hu, Q., Tian, H., 2014. Temperature changes in central Asia from 1979 to 2011 based on multiple datasets. J. Clim. 27, 1143–1167. https://doi.org/10.1175/JCLI-D-13-00064.1.

Huang, Y., Liu, H., Yu, B., Wu, J., Kang, E.L., Xu, M., Wang, S., Klein, A., Chen, Y., 2018. Improving MODIS snow products with a HMRF-based spatio-temporal modeling technique in the Upper Rio Grande Basin. Remote Sens. Environ. 204, 568–582. https://doi.org/10.1016/j.rse.2017.10.001.

Immerzeel, W.W., Droogers, P., de Jong, S.M., Bierkens, M.F.P., 2009. Large-scale monitoring of snow cover and runoff simulation in Himalayan river basins using remote sensing. Remote Sens. Environ. 113, 40–49. https://doi.org/10.1016/j.rse.2008.08.010.

Jafarov, E.E., Nicolsky, D.J., Romanovsky, V.E., Walsh, J.E., Panda, S.K., Serreze, M.C., 2014. The effect of snow: How to better model ground surface temperatures. Cold Reg. Sci. Technol. 102, 63–77. https://doi.org/10.1016/j.coldregions.2014.02.007.

Jennings, K.S., Winchell, T.S., Livneh, B., Molotch, N.P., 2018. Spatial variation of the rain–snow temperature threshold across the Northern Hemisphere. Nat. Commun. 1148, 1–9. https://doi.org/10.1038/s41467-018-03629-7.

Jordan, R., 1991. A one-dimensional temperature model for a snow cover: Technical documentation for SNTHERM. 89 (No. CRREL-SR-91-16). Cold Regions Research and Engineering Lab Hanover NH.

Kain, J.S., 2004. The Kain-Fritsch convective parameterization: an update. J. Appl. Meteorol. 43, 170–181. https://doi.org/10.1175/1520-0450(2004)043<0170:TKCPAU>2.0.CO;2.

Kumar, S., Mocko, D., Vuyovich, C., Peters-Lidard, C., 2020. Impact of surface albedo assimilation on snow estimation. Remote Sens. 12, 1–27. https://doi.org/10.3390/rs12040645.

Kumar, S. V., M. Mocko, D., Wang, S., Peters-Lidard, C.D., Borak, J., 2019. Assimilation of Remotely Sensed Leaf Area Index into the Noah-MP Land Surface Model: Impacts on Water and Carbon Fluxes and States over the Continental United States. J. Hydrometeorol. 20, 1359–1377. https://doi.org/10.1175/jhm-d-18-0237.1.

Landerer, F.W., Swenson, S.C., 2012. Accuracy of scaled GRACE terrestrial water storage estimates. Water Resour. Res. 48, 1–11. https://doi.org/10.1029/2011WR011453.

Leung, L.R., Qian, Y., 2003. The sensitivity of precipitation and snowpack simulations to model resolution via nesting in regions of complex terrain. J. Hydrometeorol. 4, 1025–1043. https://doi.org/10.1175/1525-7541(2003)004<1025:TSOPAS>2.0.CO;2.

Li, Q., Yang, T., Qi, Z., Li, L., 2018a. Spatiotemporal variation of snowfall to precipitation ratio and its implication on water resources by a regional climate model over Xinjiang, China. Water 10. https://doi.org/10.3390/w10101463.

Li, Q., Yang, T., Zhang, F., Qi, Z., Li, L., 2018b. Snow depth reconstruction over last

century: trend and distribution in the Tianshan Mountains. China. Glob. Planet. Change 173, 73–82. https://doi.org/10.1016/J.GLOPLACHA.2018.12.008.

Li, Q., Yang, T., Zhou, H., Li, L., 2019. Patterns in snow depth maximum and snow cover days during 1961–2015 period in the Tianshan Mountains, Central Asia. Atmos. Res. 228, 14–22. https://doi.org/10.1016/j.atmosres.2019.05.004.

Lievens, H., Demuzere, M., Marshall, H.P., Reichle, R.H., Brucker, L., Brangers, I., de Rosnay, P., Dumont, M., Girotto, M., Immerzeel, W.W., Jonas, T., Kim, E.J., Koch, I., Marty, C., Saloranta, T., Schöber, J., De Lannoy, G.J.M., 2019. Snow depth variability in the Northern Hemisphere mountains observed from space. Nat. Commun. 10, 1–12. https://doi.org/10.1038/s41467-019-12566-y.

Link, T.E., Marks, D., 1999. Point simulation of seasonal snow cover dynamics beneath boreal forest canopies. J. Geophys. Res. Atmos. 104, 27841–27857. https://doi.org/10.1029/1998JD200121.

Liu, C., Ikeda, K., Thompson, G., Rasmussen, R., Dudhia, J., 2011. High-resolution simulations of wintertime precipitation in the Colorado Headwaters Region: sensitivity to physics parameterizations. Mon. Weather Rev. 139, 3533–3553. https://doi.org/10.1175/MWR-D-11-00009.1.

Liu, L., Ma, Y., Menenti, M., Zhang, X., Ma, W., 2019. Evaluation of WRF modeling in relation to different land surface schemes and initial and boundary conditions: a snow event simulation over the Tibetan Plateau. J. Geophys. Res. Atmos. 124, 209–226. https://doi.org/10.1029/2018JD029208.

Liu, Z., Liu, Y., Wang, S., Yang, X., Wang, L., Baig, M.H.A., Chi, W., Wang, Z., 2018. Evaluation of spatial and temporal performances of ERA-interim precipitation and temperature in Mainland China. J. Clim. 31, 4347–4365. https://doi.org/10.1175/JCLI-D-17-0212.1.

Lu, H., Liu, M.Z., Han, X., 2017. The effects of forest litter on snow energy budget in the Tianshan Mountains. China. Hydrol. Process. 31, 1602–1612. https://doi.org/10.1002/hyp.11129.

Lu, X., Tang, G., Wang, X., Liu, Y., Jia, L., Xie, G., Li, S., Zhang, Y., 2019. Correcting GPM IMERG precipitation data over the Tianshan Mountains in China. J. Hydrol. 575, 1239–1252. https://doi.org/10.1016/j.jhydrol.2019.06.019.

Ma, X., Jin, J., Liu, J., Niu, G.-Y., 2019. An improved vegetation emissivity scheme for land surface modeling and its impact on snow cover simulations. Clim. Dyn. https://doi.org/10.1007/s00382-019-04924-9.

Malmros, J.K., Mernild, S.H., Wilson, R., Tagesson, T., Fensholt, R., 2018. Snow cover and snow albedo changes in the central Andes of Chile and Argentina from daily MODIS observations (2000–2016). Remote Sens. Environ. 209, 240–252. https://doi.org/10.1016/j.rse.2018.02.072.

Marks, D.G., Reba, M., Pomeroy, J., Link, T., Winstral, A., Flerchinger, G., Elder, K., 2008. Comparing simulated and measured sensible and latent heat fluxes over snow under a pine canopy to improve an energy balance snowmelt model. J. Hydrometeorol. 9, 1506–1522. https://doi.org/10.1175/2008JHM874.1.

Martin, K.A., Van Stan, J.T., Dickerson-Lange, S.E., Lutz, J.A., Berman, J.W., Gersonde, R., Lundquist, J.D., 2013. Development and testing of a snow interceptometer to quantify canopy water storage and interception processes in the rain/snow transition zone of the North Cascades, Washington, USA. Water Resour. Res. 49, 3243–3256. https://doi.org/10.1002/wrcr.20271.

Matthew, S., A, G.M., Charles, P., 2017. Water and life from snow: A trillion dollar science question. Water Resour. Res. 3534–3544. https://doi.org/10.1002/2017WR020840. Received.

Mazzotti, G., Essery, R., Moeser, C.D., Jonas, T., 2020. Resolving small-scale forest snow patterns using an energy balance snow model with a one-layer canopy. Water Resour. Res. 56. https://doi.org/10.1029/2019WR026129.

Meng, X., Lyu, S., Zhang, T., Zhao, L., Li, Z., Han, B., Li, S., Ma, D., Chen, H., Ao, Y., Luo, S., Shen, Y., Guo, J., Wen, L., 2018. Simulated cold bias being improved by using MODIS time-varying albedo in the Tibetan Plateau in WRF model. Environ. Res. Lett. 13. https://doi.org/10.1088/1748-9326/aab44a.

Minder, J.R., Letcher, T.W., Skiles, S.M.K., 2016. An evaluation of high-resolution regional climate model simulations of snow cover and albedo over the rocky mountains, with implications for the simulated snow-albedo feedback. J. Geophys. Res. 121, 9069–9088. https://doi.org/10.1002/2016JD024995.

Mlawer, E.J., Taubman, S.J., Brown, P.D., Iacono, M.J., Clough, S.A., 1997. Radiative transfer for inhomogeneous atmospheres: RRTM, a validated correlated-k model for the longwave. J. Geophys. Res. 102, 16663. https://doi.org/10.1029/97JD00237.

Monin, A.S., Obukhov, A.M., 1959. Basic laws of turbulent mixing in the surface layer of the atmosphere. Tr Akad Nauk SSSR Geofiz Inst 24, 163–187.

Niu, G.Y., Yang, Z.L., 2007. An observation-based formulation of snow cover fraction and its evaluation over large North American river basins. J. Geophys. Res. Atmos. 112, 1–14. https://doi.org/10.1029/2007JD008674.

Niu, G.Y., Yang, Z.L., 2004. Effects of vegetation canopy processes on snow surface energy and mass balances. J. Geophys. Res. 109, 1–15. https://doi.org/10.1029/2004JD004884.

Niu, G.Y., Yang, Z.L., Mitchell, K.E., Chen, F., Ek, M.B., Barlage, M., Kumar, A., Manning, K., Niyogi, D., Rosero, E., Tewari, M., Xia, Y., 2011. The community Noah land surface model with multiparameterization options (Noah-MP): 1. Model description and evaluation with local-scale measurements. J. Geophys. Res. Atmos. 116, 1–19. https://doi.org/10.1029/2010JD015139.

Nogueira, M., 2020. Inter-comparison of ERA-5, ERA-interim and GPCP rainfall over the last 40 years: Process-based analysis of systematic and random differences. J. Hydrol. 583, 124632. https://doi.org/10.1016/j.jhydrol.2020.124632.

Norris, J., Carvalho, L.M.V., Jones, C., Cannon, F., 2018. Deciphering the contrasting climatic trends between the central Himalaya and Karakoram with 36 years of WRF simulations. Clim. Dyn. 1–22. https://doi.org/10.1007/s00382-018-4133-3.

Norris, J., Carvalho, L.M.V., Jones, C., Cannon, F., 2015. WRF simulations of two extreme snowfall events associated with contrasting extratropical cyclones over the western and central Himalaya. J. Geophys. Res. 120, 3114–3138. https://doi.org/10.1002/2014JD022592.

Norris, J., Carvalho, L.M.V., Jones, C., Cannon, F., Bookhagen, B., Palazzi, E., Tahir, A.A., 2017. The spatiotemporal variability of precipitation over the Himalaya: evaluation of one-year WRF model simulation. Clim. Dyn. 49, 2179–2204. https://doi.org/10.1007/s00382-016-3414-y.

Pan, M., Sheffield, J., Wood, E.F., Mitchell, K.E., Houser, P.R., Schaake, J.C., Robock, A., Lohmann, D., Cosgrove, B., Duan, Q., Luo, L., Higgins, R.W., Pinker, R.T., Tarpley, J.D., 2003. Snow process modeling in the North American Land Data Assimilation System (NLDAS): 2. Evaluation of model simulated snow water equivalent. J. Geophys. Res. 108, 8850. https://doi.org/10.1029/2003JD003994.

Piao, S., Wang, X., Park, T., Chen, C., Lian, X., He, Y., Bjerke, J.W., Chen, A., Ciais, P., Tømmervik, H., Nemani, R.R., Myneni, R.B., 2020. Characteristics, drivers and feedbacks of global greening. Nat. Rev. Earth Environ. 1, 14–27. https://doi.org/10.1038/s43017-019-0001-x.

Pomeroy, J.W., Marks, D., Link, T., Ellis, C., Hardy, J., Rowland, A., Granger, R., 2009. The impact of coniferous forest temperature on incoming longwave radiation to melting snow. Hydrol. Process. 23, 2513–2525. https://doi.org/10.1002/hyp.

Pritchard, D.M.W., Forsythe, N., Fowler, H.J., O'Donnell, G.M., Li, X.F., 2019. Evaluation of upper indus near-surface climate representation by WRF in the High Asia Refined Analysis. J. Hydrometeorol. 20, 467–487. https://doi.org/10.1175/JHM-D-18-0030.1.

Qiu, Y., Hu, Q., Zhang, C., 2017. WRF simulation and downscaling of local climate in Central Asia. Int. J. Climatol. 37, 513–528. https://doi.org/10.1002/joc.5018.

Roth, T.R., Nolin, A.W., 2017. Forest impacts on snow accumulation and ablation across an elevation gradient in a temperate montane environment. Hydrol. Earth Syst. Sci. 21, 5427–5442. https://doi.org/10.5194/hess-21-5427-2017.

Rutter, N., Essery, R., Pomeroy, J., Altimir, N., Andreadis, K., Baker, I., Barr, A., Bartlett, P., Boone, A., Deng, H., Douville, H., Dutra, E., Elder, K., Ellis, C., Feng, X., Gelfan, A., Goodbody, A., Gusev, Y., Gustafsson, D., Hellström, R., Hirabayashi, Y., Hirota, T., Jonas, T., Koren, V., Kuragina, A., Lettenmaier, D., Li, W.P., Luce, C., Martin, E., Nasonova, O., Pumpanen, J., Pyles, R.D., Samuelsson, P., Sandells, M., Schädler, G., Shmakin, A., Smirnova, T.G., Stähli, M., Stöckli, R., Strasser, U., Su, H., Suzuki, K., Takata, K., Tanaka, K., Thompson, E., Vesala, T., Viterbo, P., Wiltshire, A., Xia, K., Xue, Y., Yamazaki, T., 2009. Evaluation of forest snow processes models (SnowMIP2). J. Geophys. Res. Atmos. 114. https://doi.org/10.1029/2008JD011063.

Schweizer, J., Jamieson, J.B., Schneebeli, M., 2003. Snow avalanche formation. Rev. Geophys. 41. https://doi.org/10.1029/2002RG000123.

Sicart, J.E., Pomeroy, J.W., Essery, R.L.H., Hardy, J., Link, T., Marks, D., 2004. A sensitivity study of daytime net radiation during snowmelt to forest canopy and atmospheric conditions. J. Hydrometeorol. 5, 774–784. https://doi.org/10.1175/1525-7541(2004)005 < 0774:ASSODN > 2.0.CO;2.

Skamarock, William C., Klemp, Joseph B., 2008. A time-split nonhydrostatic atmospheric model for weather research and forecasting applications. J. Comput. Phys. 227 (7), 3465–3485.

Skiles, S.M.K., Flanner, M., Cook, J.M., Dumont, M., Painter, T.H., 2018. Radiative forcing by light-absorbing particles in snow. Nat. Clim. Chang. 8, 964–971. https://doi.org/10.1038/s41558-018-0296-5.

Sorg, A., Bolch, T., Stoffel, M., Solomina, O., Beniston, M., 2012. Climate change impacts on glaciers and runoff in Tien Shan (Central Asia). Nat. Clim. Chang. 2, 725–731. https://doi.org/10.1038/nclimate1592.

Sun, S., Jin, J., Xue, Y., 1999. A simple snow-atmosphere-soil transfer model. J. Geophys. Res. Atmos. 104, 19587–19597. https://doi.org/10.1029/1999JD900305.

Tang, Z., Wang, Xiaoru, Wang, J., Wang, Xin, Li, H., Jiang, Z., 2017. Spatiotemporal variation of snow cover in Tianshan Mountains, Central Asia, based on cloud-free MODIS fractional snow cover product, 2001–2015. Remote Sens. 9, 2001–2015. https://doi.org/10.3390/rs9101045.

Taylor, K.E., 2001. Summarizing multiple aspects of model performance in a single diagram. J. Geophys. Res. 106, 7183–7192. https://doi.org/10.1029/2000JD900719.

Terzago, S., Andreoli, V., Arduini, G., Balsamo, G., Campo, L., Cassardo, C., Cremonese, E., Dolia, D., Gabellani, S., von Hardenberg, J., Morra di Cella, U., Palazzi, E., Piazzi, G., Pogliotti, P., Provenzale, A., 2020. Sensitivity of snow models to the accuracy of meteorological forcings in mountain environments. Hydrol. Earth Syst. Sci. 24, 4061–4090. https://doi.org/10.5194/hess-24-4061-2020.

Teuling, A.J., Taylor, C.M., Meirink, J.F., Melsen, L.A., Miralles, D.G., Van Heerwaarden, C.C., Vautard, R., Stegehuis, A.I., Nabuurs, G.J., De Arellano, J.V.G., 2017. Observational evidence for cloud cover enhancement over western European forests. Nat. Commun. 8, 1–7. https://doi.org/10.1038/ncomms14065.

Todt, M., Rutter, N., Fletcher, C.G., Wake, and L.M., 2019. Simulated single-layer forest canopies delay Northern Hemisphere snowmelt. Cryosph. 13, 3077–3091. https://doi.org/10.5194/tc-13-3077-2019.

Tomasi, E., Giovannini, L., Zardi, D., de Franceschi, M., 2017. Optimization of Noah and Noah_MP WRF land surface schemes in snow-melting conditions over complex terrain. Mon. Weather Rev. 145, 4727–4745. https://doi.org/10.1175/MWR-D-16-0408.1.

Tomaszewska, M.A., Nguyen, L.H., Henebry, G.M., 2020. Land surface phenology in the highland pastures of montane Central Asia: interactions with snow cover seasonality and terrain characteristics. Remote Sens. Environ. 240, 111675. https://doi.org/10.1016/j.rse.2020.111675.

Varhola, A., Coops, N.C., Weiler, M., Moore, R.D., 2010. Forest canopy effects on snow accumulation and ablation: an integrative review of empirical results. J. Hydrol. 392, 219–233. https://doi.org/10.1016/j.jhydrol.2010.08.009.

Wahr, J., Swenson, S., Velicogna, I., 2006. Accuracy of GRACE mass estimates. Geophys. Res. Lett. 33, 1–5. https://doi.org/10.1029/2005GL025305.

Wang, R., Chen, J.M., Pavlic, G., Arain, A., 2016. Improving winter leaf area index estimation in coniferous forests and its significance in estimating the land surface albedo. ISPRS J. Photogramm. Remote Sens. 119, 32–48. https://doi.org/10.1016/j.

isprsjprs.2016.05.003.

Wang, T., Peng, S., Lin, X., Chang, J., 2013. Declining snow cover may affect spring phenological trend on the Tibetan Plateau. Proc. Natl. Acad. Sci., https://doi.org/10.1073/pnas.1306157110.

Wang, W., Yang, K., Zhao, L., Zheng, Z., Lu, H., Mamtimin, A., 2020. Characterizing surface albedo of shallow fresh snow and its importance for snow ablation on the interior of the Tibetan Plateau. J. Hydrometeorol. 1–37. https://doi.org/10.1175/JHM-D-19-0193.1.

Wang, X., Wu, C., Peng, D., Gonsamo, A., Liu, Z., 2018. Snow cover phenology affects alpine vegetation growth dynamics on the Tibetan Plateau: satellite observed evidence, impacts of different biomes, and climate drivers. Agric. For. Meteorol. 256–257, 61–74. https://doi.org/10.1016/j.agrformet.2018.03.004.

Wang, Y.H., Broxton, P., Fang, Y., Behrangi, A., Barlage, M., Zeng, X., Niu, G.Y., 2019. A wet-bulb temperature-based rain-snow partitioning scheme improves snowpack prediction over the drier western united states. Geophys. Res. Lett. 46, 13825–13835. https://doi.org/10.1029/2019GL085722.

Webster, E., Ramp, D., Kingsford, R.T., 2016. Spatial sensitivity of surface energy balance algorithms to meteorological data in a heterogeneous environment. Remote Sens. Environ. 187, 294–319. https://doi.org/10.1016/j.rse.2016.10.019.

Wen, X., Lu, S., Jin, J., 2012. Integrating remote sensing data with WRF for improved simulations of oasis effects on local weather processes over an Arid Region in Northwestern China. J. Hydrometeorol. 13, 573–587. https://doi.org/10.1175/JHM-D-10-05001.1.

Winter, K.J.P.M., Kotlarski, S., Scherrer, S.C., Schär, C., 2017. The Alpine snow-albedo feedback in regional climate models. Clim. Dyn. 48, 1109–1124. https://doi.org/10.1007/s00382-016-3130-7.

Woldemichael, A.T., Hossain, F., Pielke, R., Beltrán-Przekurat, A., 2012. Understanding the impact of dam-triggered land use/land cover change on the modification of extreme precipitation. Water Resour. Res. 48. https://doi.org/10.1029/2011WR011684.

Wrzesien, M.L., Durand, M.T., Pavelsky, T.M., Kapnick, S.B., Zhang, Y., Guo, J., Shum, C.K., 2018. A new estimate of North American Mountain Snow accumulation from regional climate model simulations. Geophys. Res. Lett. 45, 1423–1432. https://doi.org/10.1002/2017GL076664.

Wu, S., Zhang, X., Du, J., Zhou, X., Tuo, Y., Li, R., Duan, Z., 2019. The vertical influence of temperature and precipitation on snow cover variability in the Central Tianshan Mountains, Northwest China. Hydrol. Process. 1–12. https://doi.org/10.1002/hyp.13431.

Xiao, Z., Liang, S., Wang, J., Chen, P., Yin, X., Zhang, L., Song, J., 2014. Use of general regression neural networks for generating the GLASS leaf area index product from time-series MODIS surface reflectance. IEEE Trans. Geosci. Remote Sens. 52, 209–223. https://doi.org/10.1109/TGRS.2013.2237780.

Xiao, Z., Liang, S., Wang, J., Xiang, Y., Zhao, X., Song, J., 2016. Long-time-series global land surface satellite leaf area index product derived from MODIS and AVHRR surface reflectance. IEEE Trans. Geosci. Remote Sens. 54, 5301–5318. https://doi.org/10.1109/TGRS.2016.2560522.

Xu, M., Liang, X.Z., Samel, A., Gao, W., 2014. MODIS consistent vegetation parameter specifications and their impacts on regional climate simulations. J. Clim. 27, 8578–8596. https://doi.org/10.1175/JCLI-D-14-00082.1.

Yang, T., Li, Q., Ahmad, S., Zhou, H., Li, L., 2019a. Changes in snow phenology from 1979 to 2016 over the Tianshan Mountains, Central Asia. Remote Sens. 11, 499. https://doi.org/10.3390/rs11050499.

Yang, T., Li, Q., Chen, X., De Maeyer, P., Yan, X., Liu, Y., Zhao, T., Li, L., 2020. Spatiotemporal variability of the precipitation concentration and diversity in Central Asia. Atmos. Res. 241, 104954. https://doi.org/10.1016/j.atmosres.2020.104954.

Yang, T., Li, Q., Liu, W., Liu, X., Li, L., De Maeyer, P., 2019b. Spatiotemporal variability of snowfall and its concentration in northern Xinjiang, Northwest China. Theor. Appl. Climatol. 1–13. https://doi.org/10.1007/s00704-019-02994-7.

Yang, Z.L., Niu, G.Y., Mitchell, K.E., Chen, F., Ek, M.B., Barlage, M., Longuevergne, L., Manning, K., Niyogi, D., Tewari, M., Xia, Y., 2011. The community Noah land surface model with multiparameterization options (Noah-MP): 2. Evaluation over global river basins. J. Geophys. Res. Atmos. 116, 1–16. https://doi.org/10.1029/2010JD015140.

Ye, B., Yang, D., Ding, Y., Han, T., Koike, T., 2005. A bias-corrected precipitation climatology for China. J. Hydrometeorol. 5, 1147–1160. https://doi.org/10.1175/jhm-366.1.

You, Y., Huang, C., Gu, J., Li, H., Hao, X., Hou, J., 2020a. Assessing snow simulation performance of typical combination schemes within Noah-MP in northern Xinjiang. China. J. Hydrol. 581, 124380. https://doi.org/10.1016/j.jhydrol.2019.124380.

You, Y., Huang, C., Yang, Z., Zhang, Y., Bai, Y., Gu, J., 2020b. Assessing Noah-MP parameterization sensitivity and uncertainty interval across snow climates. J. Geophys. Res. Atmos. 1–20. https://doi.org/10.1029/2019jd030417.

Yu, E.T., 2013. High-resolution seasonal snowfall simulation over Northeast China. Chinese Sci. Bull. 58, 1412–1419. https://doi.org/10.1007/s11434-012-5561-9.

Zhang, F., Ahmad, S., Zhang, H., Zhao, X., Feng, X., Li, L., 2016. Simulating low and high streamflow driven by snowmelt in an insufficiently gauged alpine basin. Stoch. Environ. Res. Risk Assess. 30, 59–75. https://doi.org/10.1007/s00477-015-1028-2.

Zhang, Y., Kang, S., Sprenger, M., Cong, Z., Gao, T., Li, C., Tao, S., Li, X., Zhong, X., Xu, M., Meng, W., Neupane, B., Qin, X., Sillanpää, M., 2018. Black carbon and mineral dust in snow cover on the Tibetan Plateau. Cryosph 12, 413–431. https://doi.org/10.3929/ETHZ-B-000225616.

Zheng, Z., Ma, Q., Jin, S., Su, Y., Guo, Q., Bales, R.C., 2019. Canopy and terrain interactions affecting snowpack spatial patterns in the Sierra Nevada of California. Water Resour. Res. 1–19. https://doi.org/10.1029/2018WR023758.

Zhou, H., Aizen, E., Aizen, V., 2017. Seasonal snow cover regime and historical change in Central Asia from 1986 to 2008. Glob. Planet. Change 148, 192–216. https://doi.org/10.1016/j.gloplacha.2016.11.011.